

Channel Estimation and Hybrid Precoding for Massive MIMO-OTFS System With Doubly Squint

Mingming Duan, Pengfei Zhang, Shun Zhang, *Senior Member, IEEE*,
Yao Ge, *Member, IEEE*, Octavia A. Dobre, *Fellow, IEEE* and Chau Yuen, *Fellow, IEEE*

Abstract—Orthogonal time frequency space (OTFS) modulation and massive multi-input multi-output (MIMO) are promising technologies for next generation wireless communication systems for their abilities to counteract the issue of high mobility with large Doppler spread and mitigate the channel path attenuation, respectively. The natural integration of massive MIMO with OTFS in millimeter-wave systems can improve communication data rate and enhance the spectral efficiency. However, when transmitting wideband signals with large-scale arrays, the beam squint effect may occur, causing discrepancies in beam directions across subcarriers in multi-carrier systems. Moreover, the high-mobility wideband millimeter wave communications can induce the Doppler squint effect, leading to different Doppler shifts among the subcarriers. Both beam squint effect and Doppler squint effect (denoted as doubly squint effect) can degrade communication performance significantly. In this paper, we present an efficient channel estimation and hybrid precoding scheme to address the doubly squint effect in massive MIMO-OTFS systems. We first characterize the wideband channel model and the input-output relationship for massive MIMO-OTFS transmission considering doubly squint effect. We then mathematically derive the impact of channel parameters on chirp pilots under the doubly squint effect. Additionally, we develop a peak-index-based channel estimation scheme. By leveraging the results from channel estimation, we propose a hybrid precoding method to mitigate the doubly squint effect in downlink transmission scenarios. Finally, simulation results validate the effectiveness of our proposed scheme and show its superiority over the existing schemes.

Index Terms—OTFS, massive MIMO, beam squint, Doppler squint, chirp sequence, channel estimation, hybrid precoding.

I. INTRODUCTION

Manuscript received 6 November, 2024; revised 19 February, 2025 and 28 March, 2025, accepted 7 April, 2025; date of current version 7 April, 2025. The work of M. Duan, P. Zhang and S. Zhang was supported by the National Key Research and Development Program of China under Grant 2023YFB2904500 and the National Natural Science Foundation of China under Grant 62271373. The work of Yao Ge was supported by the RIE2020 Industry Alignment Fund-Industry Collaboration Projects (IAF-ICP) Funding Initiative, as well as cash and in-kind contribution from the industry partner(s). (Corresponding author: Shun Zhang.)

Mingming Duan, Pengfei Zhang and Shun Zhang are with the State Key Laboratory of Integrated Services Networks, Xidian University, 710071, China (e-mail: duanmingming@stu.xidian.edu.cn; zhang_pengfei@stu.xidian.edu.cn; zhangshunsdu@xidian.edu.cn).

Yao Ge is with Continental-NTU Corporate Laboratory, Nanyang Technological University, Singapore 637553 (e-mail: yao.ge@ntu.edu.sg).

Octavia A. Dobre is with the Faculty of Engineering and Applied Science, Memorial University, St. Johns, NL A1B 3X5, Canada (e-mail: odobre@mun.ca).

Chau Yuen is with the School of Electrical and Electronics Engineering, Nanyang Technological University, Singapore 639798 (e-mail: chau.yuen@ntu.edu.sg).

FUTURE wireless networks are anticipated to achieve high-throughput multi-user access in high-mobility scenarios. This demand drives the exploration of millimeter wave (mmWave) communication, which is capable of utilizing the 30 to 300 GHz frequency range [1]. Despite mmWave capability of delivering multigigabit data rate, its high carrier frequency results in server path loss in comparison to systems operating in the sub-6 GHz frequency range [2], [3]. On the other hand, the reduction in wavelength of mmWave systems facilitates a high density of antennas within compact spaces. This advantage further accelerates the deployment of massive multi-input multi-output (MIMO) technology [4]. In this case, the path loss can be compensated through the use of directional beams and high array gains. Considering these characteristics, researchers have investigated to exploit the potential of massive MIMO in mmWave systems. In [5], Zhang *et al.* proposed beamforming schemes based on the reciprocity of dominant angle of arrival (AoA), where the overhead of beamforming is reduced effectively. In [6], Almoneer *et al.* deployed a hardware platform that incorporates different variants of zero-forcing precoding to investigate the performance of MIMO transmitters. Moreover, the capacity of massive user access in massive MIMO systems supports the implementation of distributed edge computing and federated learning in wireless communications [7], [8]. Cai *et al.* proposed a massive NOMA scheme for uplink and downlink transmissions in cellular IoT communications [9]. Furthermore, a low-complexity architecture is considered in hybrid precoding structures for massive MIMO systems [10]–[12]. These structures are cable of reducing the usage of the radio frequency (RF) chains and can also maintain the full multiplexing gains by using the inherent sparsity of wireless channel [10]–[13]. In [14], Ramadan *et al.* proposed a hybrid precoder design leveraging artificial noise and further investigated the impact of phase shifters (PSs) resolution. In [15], Gu *et al.* examined the relationship between the spectral efficiency, interleaved structures, and antenna spacing, where an optimal interval for hybrid precoding design was proposed for subconnected architectures.

On the other hand, in wideband systems equipped with a substantial number of antennas, the propagation delay variation among antennas can be comparable to the sampling period, making the time delay across the array non-negligible. This phenomenon can further lead to the beam squint effect [16], resulting the beam direction to vary with subcarriers for the transmission of multi-carrier signals [17]–[19]. Due to the loss of the array gain along the subcarriers, the traditional beamforming algorithms exhibit a significant performance

degradation [20]. Fortunately, the beam squint effect can be compensated for either at the receiver or transmitter. Specifically, on the receiver side, the communication performance can be improved primarily by improving channel estimation techniques in the context of beam squint effect. In [21], Maity *et al.* proposed a channel estimation scheme utilizing dictionary-learning based to counteracts beam squint effect. In [22], Shi *et al.* proposed a frequency-dependent estimation method to minimize the beam squint effect, where a frequency dependent dictionary was established for each subcarrier. At the transmitter side, extensive studies have been dedicated to mitigate the reduction in array gain resulting from the beam squint effect. In [23], Cai *et al.* developed a codebook design that maximizes the array gain across all subcarriers to mitigate the beam squint effect. In [24], Zhang *et al.* proposed an alternative iterative algorithm for both fully connected and subconnected array architectures to alleviate the effect of beam squint and enhance the average rate. In [25], Dai *et al.* introduced a delay-phase precoding (DPP) to reduce the loss of array gain experienced over the entire bandwidth.

Doppler caused by mobility between transmitter and receiver is another notable factor in wireless communication. It results in a time-varying channel with significant changes in both amplitude and phase over time [26]. Therefore, the performance of the modulation technique employed in 4G and 5G networks, i.e., orthogonal frequency division multiplexing (OFDM), may deteriorate due to the degradation of orthogonality among subcarriers. Fortunately, Hadani *et al.* proposed orthogonal time frequency space (OTFS) modulation [27], which can exploit the diversity of both channel delays and Doppler spreads. OTFS demonstrates a distinct advantage over OFDM in high mobility communications with large Doppler spread. By integrating OTFS with massive MIMO systems, the channel can be further scheduled in a three-dimensional (3-D) Doppler-delay-angle domain for performance enhancement with pertinent resource allocation schemes [28], [29]. In [30], Pandey *et al.* presented a multi-user precoder and detector for massive MIMO-OTFS system, where the complexity was reduced by independently performing detection for each information symbol. In [31], Shao *et al.* introduced a 3-D non-orthogonal multiple access scheme to exploit the delay-Doppler domain resources with the overlapped angle signature. In [32], Shen *et al.* adapted massive MIMO-OTFS for satellite communications to address the issues arising from high mobility and massive access in satellite-based communications. In [33], Li *et al.* constructed a path division multiple access (PDMA) scheme, which fully utilizes the scattering path resolution by assigning angle-domain resources to different users.

However, in the case of wideband signal transmissions, the high mobility can cause Doppler squint effect (DSE), resulting in frequency-dependent Doppler shifts. This effect can particularly disrupt sparsity of the channel, leading to inaccuracy in channel estimation and data detection because of modeling error. Most of the current research on OTFS assumes the channel exhibits substantial sparsity in the DD domain, where the DSE is not considered. Nonetheless, it has been proved that the performance of OTFS systems can be severely

compromised if DSE is disregarded [34]. For the improvement of OTFS communication performance in high-mobility wideband scenarios, it is imperative to account for the impact of DSE. In [35], Wang *et al.* proposed a parameter estimation scheme based on sparse Bayesian learning, thereby enhancing the accuracy of channel estimation for OTFS systems with DSE. In [36], Wang *et al.* emphasized the importance of accounting for DSE in OTFS systems and introduced a low-complexity receiver design incorporating linear equalization, which improves performance of OTFS in the presence of DSE.

Future communication systems with high-mobility will likely encounter both beam squint and Doppler squint effects simultaneously. Therefore, it is necessary and important to develop novel communication schemes that can effectively handle both beam squint effect and Doppler squint effect. In [37], Liao *et al.* introduced a channel estimation scheme to address performance degradation resulting from Doppler squint effect and beam squint effect for massive MIMO-OFDM systems. However, the scheme proposed in [37] can not be directly applied for massive MIMO-OTFS systems subject to high mobility challenges. In addition, the existing studies in the field of massive MIMO-OTFS systems are mainly focused on addressing either beam squint effect or Doppler squint effect separately, rather than addressing both simultaneously. In order to enhance the performance of massive MIMO-OTFS systems under future high mobility and wideband transmissions, we introduce an efficient channel estimation and hybrid precoding scheme in this work based on the doubly-squint effect, i.e., beam squint and Doppler squint channel conditions. The main contributions of our study can be summarized as follows:

- We introduce a massive MIMO-OTFS system model based on the doubly-squint effect. We derive the input-output relationship in the DD domain with the proposed hybrid precoding scheme. Meanwhile, we discuss and analyze the specific effect of Doppler squint and beam squint in wideband systems compared to narrowband systems.
- We propose a channel estimation structure based on chirp pilot and develop a parameter estimation method considering the doubly squint effect. Specifically, we mathematically derive the optimal design of true time delay (TTD) and phase shifter (PS) for chirp pilots under doubly squint effect. Additionally, we establish the relationship between peak index and channel parameters. Then we propose a peak-based channel estimation scheme.
- We propose a hybrid precoding method (including digital and analog precoding) to address the doubly squint effect. Specifically, the analog precoding addresses the beam squint effect, while the digital precoding mitigates the Doppler squint effect.
- Simulation results demonstrate that the proposed channel estimation and precoding method can achieve stronger performance than the existing methods and exhibit robustness to wideband massive MIMO-OTFS system.

The remainder of this paper is organized as follows. Section II introduces the system model of massive MIMO-OTFS,

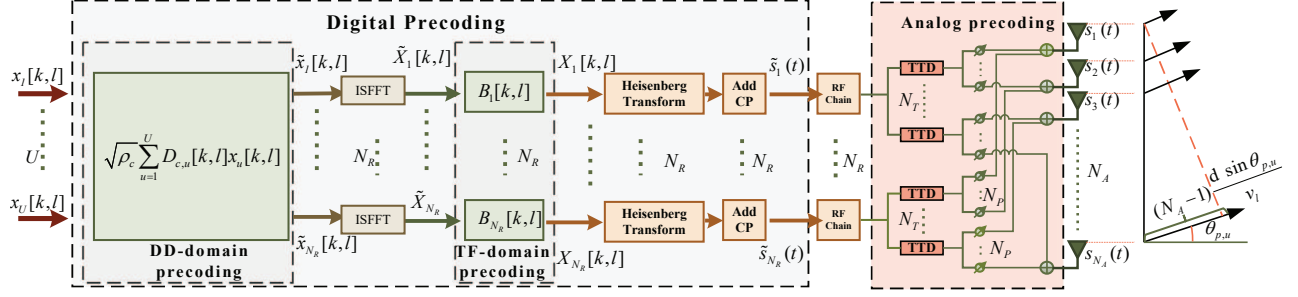


Fig. 1. Massive MIMO-OTFS system with Hybrid structure.

where the input-output relationship considering the doubly squint effect is presented. In Section III, we introduce the chirp pilot into the wideband massive MIMO system and propose a novel channel parameter estimation framework. Section IV develops the hybrid precoding schemes, which addresses the beam squint and Doppler squint effect through analog precoding and digital precoding, respectively. Simulation results are presented in Section V and the conclusions are delineated in Section VI, respectively.

Notation: $(\cdot)^*$ represents conjugate. The real part and the imaginary part of x are expressed as $\Re(x)$ and $\Im(x)$, respectively. Let $\|x\|$ denote the Euclidean norm. $\mathbb{E}(\cdot)$ represents the expectation. $|\cdot|$ is the absolute value. $(*)$ denotes convolution. $[\cdot]_N$ is the MOD N processing. Finally, $\delta(\cdot)$ represents the Dirac delta function.

II. SYSTEM MODEL

We examine a wideband mmWave massive MIMO-OTFS system, which includes a base station (BS) and U single-antenna users. It is assumed that there are P scattering paths between the BS and each user. The BS is furnished with a uniform linear array (ULA) that comprises N_A antennas and N_R RF chains. As shown in Fig. 1, each RF chain is connected to N_T independent TTDs, i.e., the TTD set connected to the c -th RF chain is defined as $\mathbf{T}_c = \{\mathbf{T}_{c,1}, \mathbf{T}_{c,2}, \dots, \mathbf{T}_{c,N_T}\}$ with $\mathbf{T}_c \cap \mathbf{T}_{c'} = \emptyset$ when $c \neq c'$, where $\mathbf{T}_{c,d}$ denotes the d -th TTD in \mathbf{T}_c , $d = 1, 2, \dots, N_T$ and $c = 1, 2, \dots, N_R$. Each TTD is then connected to $N_P = N_A/N_T$ PSs, i.e., the PS set connected to $\mathbf{T}_{c,d}$ is defined as $\mathbf{P}_{c,d} = \{\mathbf{P}_{c,d,1}, \mathbf{P}_{c,d,2}, \dots, \mathbf{P}_{c,d,N_P}\}$ with $\bigcup_{c=1}^{N_R} \bigcup_{d=1}^{N_T} \mathbf{P}_{c,d} = \Omega$ and $\mathbf{P}_{c,d} \cap \mathbf{P}_{c',d'} = \emptyset$ either when $c \neq c'$ or $d \neq d'$, where $\mathbf{P}_{c,d,s}$ denotes the s -th PS in $\mathbf{P}_{c,d}$, $s = 1, 2, \dots, N_P$ and $|\Omega| = N_A N_R$. Finally, each antenna is connected to N_R PSs, i.e., the PS set connected to the a -th antenna is defined as $\mathbf{P}'_a = \{\mathbf{P}'_{a,1}, \mathbf{P}'_{a,2}, \dots, \mathbf{P}'_{a,N_R}\}$ with $\bigcup_{a=1}^{N_A} \mathbf{P}'_a = \Omega$ and $\mathbf{P}'_a \cap \mathbf{P}'_{a'} = \emptyset$ when $a \neq a'$. Here, $\mathbf{P}'_{a,c} = \mathbf{P}_{c,d,s}$ represents the same PS for $a = (d-1)N_P + s$.

A. OTFS Transmitter

We assume that the BS can transmit independent OTFS symbols to U users simultaneously. As shown in Fig. 1, the U OTFS symbols are first processed by digital precoding, which includes DD-domain precoding and TF-domain precoding. Let $\mathbf{x}_u \in \mathbb{C}^{N \times M}$ denote OTFS symbol transmitted to the u -th user, $u = 1, 2, \dots, U$. Then, the OTFS symbols are precoded

in DD domain to generate N_R independent OTFS symbols for N_R RF chains. After DD-domain digital precoding, the OTFS symbol related to the c -th RF chain is given by

$$\tilde{x}_c[k, \ell] = \sqrt{\rho_c} \sum_{u=1}^U D_{c,u}[k, \ell] x_u[k, \ell], c = 1, \dots, N_R, \quad (1)$$

where $x_u[k, \ell]$ is the element of \mathbf{x}_u in the k -th row and ℓ -th column, $\sqrt{\rho_c}$ is the power factor and $D_{c,u}[k, \ell]$ is the DD-domain digital precoding element. With the help of the inverse symplectic finite Fourier transform (ISFFT), we can derive the TF domain symbol $\tilde{X}_c[n, m]$, i.e.,

$$\tilde{X}_c[n, m] = \frac{1}{\sqrt{NM}} \sum_{k=0}^{N-1} \sum_{\ell=0}^{M-1} \tilde{x}_c[k, \ell] e^{j2\pi(\frac{nk}{N} - \frac{m\ell}{M})}, \quad n = 0, \dots, N-1, m = 0, \dots, M-1. \quad (2)$$

Subsequently, TF-domain digital precoding is implemented to mitigate the subcarrier-dependent and time-dependent phase shifts, expressed as

$$X_c[n, m] = B_c[n, m] \tilde{X}_c[n, m], \quad (3)$$

where $B_c[n, m]$ is the TF-domain digital precoding element. We then obtain the continuous baseband time-domain signal $\tilde{s}_c(t)$ using the Heisenberg transform given by

$$\tilde{s}_c(t) = \sum_{n=0}^{N-1} \sum_{m=0}^{M-1} X_c[n, m] g_{tx}(t - nT) e^{j2\pi m \Delta f (t - nT)}, \quad (4)$$

where $g_{tx}(t)$, T and Δf denote the transmit pulse, the symbol duration and subcarrier interval, respectively. In order to counteract the effect of multipath, a cyclic prefix (CP) is added with the length exceeding the maximum delay spread.

As shown in Fig. 1, the final time-domain signal $\mathbf{s}(t) = \{s_1(t), s_2(t), \dots, s_{N_A}(t)\}^T$ can be derived by applying analog precoding to the signals from N_R RF chains. For the signal from the c -th RF chain, it is forwarded to the a -th antenna via the TTD $\mathbf{T}_{c,d}$ and the PS $\mathbf{P}'_{a,c}$ (i.e., $\mathbf{P}_{c,d,s}$). Therefore, the time-domain response from the c -th RF chain to the a -th antenna (i.e., the equivalent time-domain response introduced by $\mathbf{T}_{c,d}$ and $\mathbf{P}_{c,d,s}$) can be expressed as

$$\bar{h}_{c,d,s}(t) = \delta(t - t_{c,d}) e^{j2\pi \Psi_{c,d,s}}, \quad (5)$$

$$h_{u,a}(\tau, \nu) = \begin{cases} \sum_{p=1}^P \alpha_{p,u} e^{-j2\pi(a-1)\psi_{p,u}} \left| \frac{f_c}{\nu_{p,u}} \right| e^{2\pi \frac{f_c}{\nu_{p,u}} (\tau - \tau_{p,u} - (a-1) \frac{\psi_{p,u}}{f_c}) (\nu - \nu_{p,u})}, & \nu_{p,u} \neq 0 \\ \sum_{p=1}^P \alpha_{p,u} e^{-j2\pi(a-1)\psi_{p,u}} \delta\left(\tau - \tau_{p,u} - (a-1) \frac{\psi_{p,u}}{f_c}\right) \delta(\nu), & \nu_{p,u} = 0 \end{cases}, \quad (9)$$

where $t_{c,d}$ is the delay of the $\mathbf{T}_{c,d}$ and $e^{j2\pi\Psi_{c,d,s}}$ expresses the phase shift of $\mathbf{P}_{c,d,s}$. Thus, the a -th element of $\mathbf{s}(t)$ can be derived as

$$s_a(t) = \sum_{c=1}^{N_R} \tilde{s}_c(t - t_{c,d}) e^{j2\pi\Psi_{c,d,s}}, a = (d-1)N_P + s, \\ d = 1, 2, \dots, N_T, s = 1, 2, \dots, N_P. \quad (6)$$

B. Massive MIMO-OTFS Channel Model

In the majority of studies related to massive MIMO, channel parameters are assumed to remain constant within a snapshot. However, in wideband systems, the delay variation, which leads to the Doppler squint effect, cannot be ignored within a snapshot [34].¹ In this work, we consider a wideband channel model, where the TF-domain channel response between the a -th antenna of BS and the u -th user can be expressed as

$$H_{u,a}(t, f) = \sum_{p=1}^P \tilde{\alpha}_{p,u} e^{-j2\pi(f_c+f)\tau_{p,u,a}} e^{j2\pi \frac{\nu_{p,u}}{f_c} (f_c+f)t} \\ = \sum_{p=1}^P \tilde{\alpha}_{p,u} e^{-j2\pi(f_c+f)(\tau_{p,u,a} - \frac{\nu_{p,u}}{f_c} t)}, \quad (7)$$

where $\tilde{\alpha}_{p,u}$, $\nu_{p,u} = \frac{v_{p,u} f_c}{v_l}$ and $v_{p,u}$ denote the complex channel gain, Doppler shift and velocity of the p -th path with u -th user, respectively. v_l and f_c denote the velocity of light and the carrier frequency. $\tau_{p,u,a}$ is the propagation delay corresponding to a -th BS antenna of the p -th path with u -th user and can be written as

$$\tau_{p,u,a} = \tau_{p,u} + (a-1) \frac{d \sin(\theta_{p,u})}{f_c \lambda_c}, \quad (8)$$

where $\tau_{p,u}$ and $\theta_{p,u}$ denote the propagation delay and the physical direction the p -th path with the u -th user. d and λ_c denote the antenna spacing and carrier wavelength, respectively. In this work, we set $d = \frac{\lambda_c}{2}$ and define the spatial direction as $\psi_{p,u} = \frac{d \sin(\theta_{p,u})}{\lambda_c}$. Subsequently, the DD-domain channel response $h_{u,a}(\tau, \nu)$ can be derived by the 2D symplectic finite Fourier transform (SFFT) of $H_{u,a}(t, f)$ [34] as (9), at the top of the next page, where $\alpha_{p,u} = \tilde{\alpha}_{p,u} e^{-j2\pi f_c \tau_{p,u}}$ is the equivalent path gain.

C. OTFS Receiver

At the u -th user, the CP is first removed and the received time-domain signal can be formulated as

$$\tilde{y}_u(t) = \sum_{a=1}^{N_A} \int \int h_{u,a}(\tau, \nu) e^{j2\pi\nu(t-\tau)} s_a(t-\tau) d\tau d\nu + w_u(t), \quad (10)$$

where $w_u(t)$ is the additional white Gaussian noise (AWGN) at the u -th user with variance σ^2 . By using Wigner transform, the TF domain signal $Y_u(t, f)$ can be derived as

$$Y_u(t, f) = \int g_{rx}^*(t' - t) \tilde{y}_u(t') e^{-j2\pi f t'} dt', \quad (11)$$

where $g_{rx}(t)$ is the receive pulse. We sample the output $Y_u(t, f)$ as $Y_u[n, m] = Y_u(t, f)|_{t=nT, f=m\Delta f}$. Then, the TF-domain symbol $Y_u[n, m]$ can be represented as

$$Y_u[n, m] = \sum_{n'=0}^{N-1} \sum_{m'=0}^{M-1} \sum_{c=1}^{N_R} H_{n,m}^{u,c}[n', m'] X_c[n', m'] + W_u[n, m], \\ n = 0, 1, \dots, N-1, m = 0, 1, \dots, M-1, \quad (12)$$

where $W_u[n, m]$ is transformed and sampled from $w_u(t)$ by the Wigner transform. $H_{n,m}^{u,c}[n', m']$ is the channel matrix expressed as (13), at the top of the next page, where $A_{g_{rx}, g_{tx}}(\tau, \nu) = \int_0^T g_{tx}(t) g_{rx}^*(t - \tau) e^{-j2\pi\nu t} dt$ is the cross-ambiguity function and $\tilde{h}_{u,c}(\tau, \nu)$ is the equivalent DD-domain channel response from c -th RF chain of BS to the u -th user. $\tilde{h}_{u,c}(\tau, \nu)$ can be derived as (14) at the top of the next page by integrating (5) and (9) with $a = (d-1)N_P + s$.

Without loss of generality, both $g_{tx}(t)$ and $g_{rx}(t)$ are assumed to be rectangular pulses. Then, as described in [39], the cross-ambiguity function in (13) can be considered non-zero only for $n' = n$ or $n' = [n-1]_N$. Therefore, $Y_u[n, m]$ can be reformulated as (15), where the first item represents the ISI, the second item denotes ICI, and the third item corresponds to AWGN. By using SFFT and combining (1), (2), (3), (13) and (14), the input-output relationship in DD domain is written as

$$y_u[k, \ell] = \frac{1}{NM} \sum_{k'=0}^{N-1} \sum_{\ell'=0}^{M-1} \sum_{u'=1}^U h_{k,\ell}^{u,u'}[k', \ell'] x_{u'}[k', \ell'] + w_u[k, \ell], \quad (16)$$

where $h_{k,\ell}^{u,u'}[k', \ell']$ is given by (17) with $a = (d-1)N_P + s$. The derivation is similar to [34], [39], where we apply

$$A_{g_{rx}, g_{tx}}(t, f) \approx \frac{1}{M} \sum_{i \in Q} e^{-j2\pi f \frac{iT}{M}}, \quad (18)$$

¹According to the 3rd Generation Partnership Project (3GPP) Technical Report 38.901 [38], it is acceptable for the channel parameters to be updated within a distance variation less than 1 meter. In this paper, the distance of user moving within an OTFS symbol period and the channel estimation period can be much less than 1 meter. For the sake of simplification, Doppler and angle are still considered constant within a snapshot due to their insensitivity to bandwidth.

$$H_{n,m}^{u,c}[n',m'] = \iint \tilde{h}_{u,c}(\tau,\nu) A_{g_{rx},g_{tx}}((n-n')T - \tau, (m-m')\Delta f - \nu) e^{j2\pi(\nu-m\Delta f)(\tau+n'T)} d\tau d\nu, \quad (13)$$

$$\tilde{h}_{u,c}(\tau,\nu) = \begin{cases} \sum_{p=1}^P \sum_{a=1}^{N_A} \alpha_{p,u} e^{-j2\pi f_c(t_{c,d} + (a-1)\frac{\psi_{p,u}}{f_c})} \left| \frac{f_c}{\nu_{p,u}} \right| e^{2\pi \frac{f_c}{\nu_{p,u}} (\tau - t_{c,d} - \tau_{p,u} - (a-1)\frac{\psi_{p,u}}{f_c})} (\nu - \nu_{p,u}) e^{j2\pi \Psi_{a,b,c}}, & \nu_{p,u} \neq 0 \\ \sum_{p=1}^P \sum_{a=1}^{N_A} \alpha_{p,u} e^{-j2\pi f_c(t_{c,d} + (a-1)\frac{\psi_{p,u}}{f_c})} \delta\left(\tau - t_{c,d} - \tau_{p,u} - (a-1)\frac{\psi_{p,u}}{f_c}\right) \delta(\nu) e^{j2\pi \Psi_{a,b,c}}, & \nu_{p,u} = 0 \end{cases}, \quad (14)$$

$$Y_u[n,m] = \sum_{m'=0}^{M-1} \sum_{c=1}^{N_R} H_{n,m}^{u,c}[n-1,m'] B_c[n-1,m'] \tilde{X}[n-1,m'] + \sum_{m'=0}^{M-1} \sum_{c=1}^{N_R} H_{n,m}^{u,c}[n,m'] B_c[n,m'] \tilde{X}[n,m'] + W_u[n,m], \quad (15)$$

$$h_{k,\ell}^{u,u'}[k',\ell'] = \frac{\sqrt{\rho_c}}{MN} \sum_{n=0}^{N-1} \sum_{m=0}^{M-1} \sum_{n'=0}^{N-1} \sum_{d=1}^{N_T} \sum_{s=1}^{N_P} \sum_{c=1}^{N_R} \int \int \sum_{p=1}^P \alpha_{p,u} |\mu_{p,u}| e^{j2\pi(-\frac{nk}{N} + \frac{m\ell}{M})} e^{j2\pi \mu_{p,u}(\tau - t_{c,d} - \tau_{p,u} - (a-1)\frac{\psi_{p,u}}{f_c})(\nu - \nu_{p,u})} e^{-j2\pi \Psi_{c,d,s}} \\ \times e^{-j2\pi f_c(t_{c,d} + (a-1)\frac{\psi_{p,u}}{f_c})} \frac{1}{M} \sum_{i \in Q} e^{j2\pi i(\nu T - m)} \sum_{m'=0}^{M-1} e^{j2\pi \frac{m'(i-\ell')}{M}} e^{j2\pi \frac{n'k'}{N}} B_c[n',m'] D_{c,u'}[k',\ell'] e^{j2\pi(\nu-m\Delta f)(\tau+n'T)} d\tau d\nu \quad (17)$$

$$\tilde{h}_{k,\ell}^{u,u'}[k',\ell'] = \sum_{n=0}^{N-1} \sum_{m=0}^{M-1} \sum_{p=1}^P \sum_{c=1}^{N_R} \sum_{n'=0}^{N-1} \sum_{d=1}^{N_T} \sum_{s=1}^{N_P} \frac{\sqrt{\rho_c}}{NM} \alpha_{p,u} e^{j2\pi(\frac{n(k'-k)}{N} - \frac{m(\ell'-\ell)}{M})} e^{-j2\pi(((d-1)N_P + s-1)\psi_{p,u} + t_{c,d}f_c)(1 + \frac{m\Delta f}{f_c})} e^{j2\pi \Psi_{c,d,s}} \\ \times e^{j2\pi \nu_{p,u} \frac{(\ell' + \bar{\ell}_{c,d} + \ell_{p,u} + ((d-1)N_P + s-1)\frac{\psi_{p,u}}{f_c T_s})T}{M}} \times \begin{cases} e^{-j2\pi \frac{m\ell_{p,u}}{M}} e^{j2\pi n(\frac{k_{p,u}}{N} + \frac{m}{\mu_{p,u}})}, & \ell' \in \mathcal{L}_{ICI}^{p,u} \\ e^{-j2\pi \frac{k'\ell'}{N}} e^{-j2\pi \frac{m\ell_{p,u}}{M}} e^{j2\pi(n-1)(\frac{k_{p,u}}{N} + \frac{m}{\mu_{p,u}})}, & \ell' \in \mathcal{L}_{ISI}^{p,u} \end{cases}, \quad (20)$$

with

$$Q = \begin{cases} \{i \in \mathbb{N} : 0 \leq \frac{iT}{M} < t + T\}, t \in (-T, 0) \\ \{i \in \mathbb{N} : t \leq \frac{iT}{M} < T\}, t \in [0, T) \end{cases}. \quad (19)$$

D. Discussion of the Doubly Squint Effect

In order to illustrate the doubly squint effect in wideband massive MIMO-OTFS scenarios, we first investigate the equivalent delay-Doppler-domain channel response without involving the digital precoding (e.g., $B_c[n,m] = 1$ and $D_{c,u}[k,\ell] = 1, \forall c,u,m,n,k,\ell$). Thus, the DD-domain equivalent channel response can be simplified to $\tilde{h}_{k,\ell}^{u,u'}[k',\ell']$ as shown in (20), where $k_{p,u} = \nu_{p,u}NT$, $\ell_{p,u} = \frac{\tau_{p,u}M}{T}$, $\bar{\ell}_{c,d} = \frac{t_{c,d}}{T_s}$, $\mu_{p,u} = \frac{f_c}{\nu_{p,u}}$ and T_s is the sampling period. $\mathcal{L}_{ICI}^{p,u}$ and $\mathcal{L}_{ISI}^{p,u}$ are the index sets of the p -th path with u -th user for ICI and ISI, respectively.

Proof: Appendix A.

Equation (20) reveals that the DD-domain equivalent channel response consists of space-frequency-angle coupling $e^{\frac{-j2\pi((d-1)N_P + s-1)\psi_{p,u}m\Delta f}{f_c}}$ and time-frequency-Doppler coupling $e^{\frac{j2\pi mn}{\mu_{p,u}}}$, leading to beam squint effect and Doppler squint effect, respectively. The coupling $e^{\frac{-j2\pi((d-1)N_P + s-1)\psi_{p,u}m\Delta f}{f_c}}$ indicates that the beam squint effect introduces a phase shift depends on subcarrier and antenna. Furthermore, this coupling indicates that the beam squint effect is influenced by the number of antennas N_A , the spatial angle $\psi_{p,u}$ and the ratio of bandwidth to carrier frequency $\frac{B}{f_c}$. Thus, the beam squint effect increases when either magnitude of the spatial angle $|\psi_{p,u}|$ or the ratio $\frac{B}{f_c}$ increases. The time-frequency-Doppler coupling $e^{\frac{j2\pi mn}{\mu_{p,u}}}$ indicates that the Doppler squint effect introduces a subcarrier-dependent phase shift. Considering $\mu_{p,u} = \frac{f_c}{\nu_{p,u}} = \frac{v_l}{v_{p,u}}$, the maximum Doppler squint effect can be expressed as $\frac{MN\nu_{p,u}}{f_c} = \frac{MNv_{p,u}}{v_l}$. Therefore, the

Doppler squint effect depends on the radial velocity $v_{p,u}$ and the product $M \times N$. In practical systems, the duration of an OTFS frame is given by $T_{\text{symbol}} = NT = \frac{NM}{B}$. Consequently, the maximum Doppler squint effect can be represented as $e^{j2\pi \frac{v_{p,u} B T_{\text{symbol}}}{v_l}}$. Thus, the Doppler squint effect is determined by the radial velocity, bandwidth and symbol duration. Therefore, in wideband massive MIMO-OTFS systems with high mobility, the combined impact of Doppler squint and beam squint effect, referred to as the doubly squint effect, must be considered.

In massive MIMO-OTFS systems, we can characterize the channel in the delay-Doppler-angle domain. By using discrete Fourier transform (DFT) on $\tilde{h}_{k,\ell}^{u,u'}[k',\ell']$ with respect to the antenna index a , we can derive the delay-Doppler-angle-domain channel response as $\tilde{h}_{k,\ell,\psi}^{u,u'}[k',\ell'] = \frac{1}{\sqrt{N_A}} \sum_{a=1}^{N_A} \tilde{h}_{k,\ell}^{u,u'}[k',\ell'] e^{j2\pi \frac{a\psi}{N_A}}$, where $a = (d-1)N_P + s$ and ψ is the spatial angle in angle domain. As illustrated in Fig. 2, in narrowband and small array systems, i.e., $\frac{N_A m \Delta f}{f_c} \ll 1$ and $\frac{mn}{\mu_{p,u}} \ll 1$, the impact of space-frequency-angle coupling and time-frequency-Doppler coupling terms can be disregarded. However, in wideband massive MIMO-OTFS systems, these two coupling terms can lead to dispersion within the delay-Doppler-angle domain. Such dispersion can subsequently cause additional inter-path interference, ICI and ISI. In this work, we propose to compensate for these coupling effects by optimizing digital precoding (i.e., $D_{c,u}[k,\ell]$ and $B_c[n,m]$) and analog precoding (i.e., $t_{c,d}$ and $\Psi_{c,d,s}$) in Section IV.

III. PROPOSED UPLINK CHANNEL ESTIMATION WITH CHIRP-BASED PILOT

Before optimizing digital precoding and analog precoding, it is essential and necessary to obtain the channel parameters

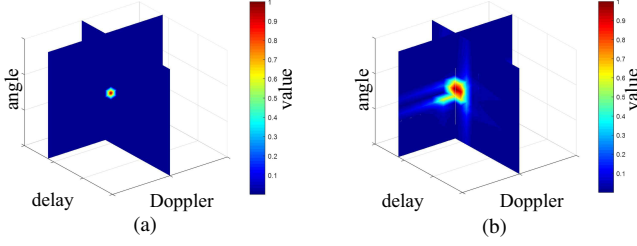


Fig. 2. Delay-Doppler-angle-domain channel response (a) in narrowband system; (b) in wideband system.

accurately. In OTFS channel estimation, embedded pilot aided estimation and preamble aided estimation are two feasible schemes. The embedded pilot scheme integrates pilot symbols into the DD domain grid directly. The receiver extracts the pilot to estimate the channel state information, which is then used for data detection [40]. The preamble-based estimation scheme inserts a known pilot sequence (i.e., preamble) at the beginning of data frame. The receiver uses this preamble to estimate the channel state, which can be used for data detection or precoding. In this work, channel estimation is not for data detection but rather for precoding design. Thus, preamble-based channel estimation is particularly suitable for this scenario.

In traditional multiuser MIMO-OTFS channel estimation, the pilots of different users are usually assigned in same DD domain symbol to realize simultaneous multiuser channel estimation [41]. However, it is infeasible in massive MIMO system with hybrid structure as the base station cannot receive the pilot in the DD domain if the angle of the user is unknown. In this paper, we propose an chirp-based channel estimation method in time division duplex (TDD) mode with angle sweeping. The chirp signal, which has superior cross-correlation properties, is widely used in radar systems. In addition, the chirp signal exhibits excellent pulse compression characteristics, thereby leading to superior estimation performance of range and Doppler [42], [43]. Leveraging these advantages, the chirp-based pilot is selected as the preamble for our channel estimation. Specifically, we first preset an angle-domain codebook with N_A angles. Each RF chain can independently receive the signal from a specific angle by controlling the PSs and TTDs. Within a TDD slot, the BS can receive signals from N_R angles simultaneously. Fig. 3 illustrates the structure of the proposed channel estimation scheme, which is comprised of two phases. The first phase is angle sweeping, during which each user sends G up-chirp pilots across $G = \left\lceil \frac{N_A}{N_R} \right\rceil$ separate TDD slots. The BS adjusts the sweeping angle of each RF chain. Following angle sweeping, the BS can derive the angle of the paths with the angle of the p -th path denoted as $\psi_{p,u}$. The second phase is beamforming receiving, where the user transmits a down-chirp pilot in $(G+1)$ -th slot. The BS RF chains align the sweeping angles to the angles estimated in angle sweeping phase. Then, the BS can receive down-chirp pilot from P scattering paths directly within a TDD slot. Consequently, the BS can calculate the DFT-angle sequences from up-chirp and down-chirp pilots.

Finally, the channel parameters can be derived with DFT-angle sequences.

In this work, the up-chirp pilot $\hat{C}[i]$ and down-chirp pilot $\check{C}[i]$ are respectively represented as

$$\hat{C}[i] = e^{j2\pi\kappa i^2}, i = 0, \dots, M-1, \quad (21)$$

$$\check{C}[i] = e^{-j2\pi\kappa i^2}, i = 0, \dots, M-1, \quad (22)$$

where M is the length of chirp sequence and $\kappa = \frac{1}{2M}$ is chirp rate [44], [45]. To mitigate the effects of the multipath, a chirp-periodic prefix (CPP) is introduced [46] as

$$\hat{C}[i] = \hat{C}[M+i]e^{j2\pi\kappa(M^2+2Mi)}, i = -N_{CPP}, \dots, -2, -1, \quad (23)$$

$$\check{C}[i] = \check{C}[M+i]e^{-j2\pi\kappa(M^2+2Mi)}, i = -N_{CPP}, \dots, -2, -1, \quad (24)$$

where N_{CPP} is the length of the CPP and surpasses the maximum delay spread. In the subsequent, we will introduce angle sweeping and beamforming receiving phases, respectively.

A. Angle Sweeping for Up-chirp Pilot

In the first phase, each user transmits an up-chirp pilot at each TDD slot and BS receives pilot from P scattering paths. Taking the g -th TDD slot with u -th user as an example, the up-chirp pilot received by the a -th antenna of the BS can be represented as

$$\tilde{r}_{a,g,u}[i] = \sum_{p=1}^P \alpha_{p,u}^g e^{j2\pi\kappa \left(i - \left(\ell_{p,u}^g + (a-1) \frac{\psi_{p,u}}{f_c T_s} - \frac{\nu_{p,u}}{f_c} i \right) \right)^2} \times e^{-j2\pi \left((a-1) \frac{\psi_{p,u}}{f_c} - \nu_{p,u} i T_s \right)} + \tilde{w}_{a,g,u}[i], i = 0, 1, \dots, M-1, \quad (25)$$

where $\alpha_{p,u}^g = \tilde{\alpha}_{p,u} e^{-j2\pi f_c (\tau_{p,u} - \frac{\nu_{p,u}}{f_c} (g-1)(M+N_{CPP})T_s)}$ is the path gain at the g -th slot and $\tilde{w}_{a,g,u}[i]$ is the AWGN at the a -th BS antenna for the estimation period of the u -th user. ² $\ell_{p,u}^g$ is the delay at the g -th slot and can be expressed as

$$\ell_{p,u}^g = \ell_{p,u} - \frac{\nu_{p,u}}{f_c} (M + N_{CPP})(g-1). \quad (26)$$

The processes illustrated in Fig. 4 is then implemented.

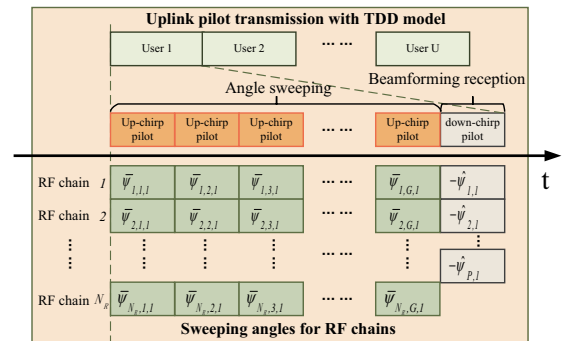


Fig. 3. Proposed channel estimation scheme with TDD model.

²Doppler squint effect can be represented as a time-varying delay in the time-domain channel response [34], (i.e., $h(t) = \sum_{p=1}^P \alpha_p(t) \delta(t - \tau_p(t))$), where $\tau_p(t) = \tau_p - \frac{\nu_p}{f_c} t$. Taking into account the effect of time-varying delay, the gain and delay in each TDD slot should be considered different.

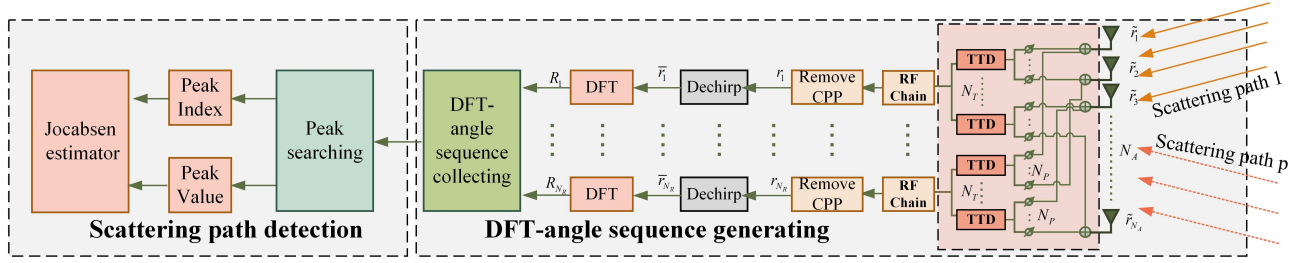


Fig. 4. Angle sweeping process for up-chirp pilot.

1) *DFT-angle Sequence Generating*: With respect to the c -th RF chain, the BS adjusts the sweeping angle of this RF chain by optimizing the TTD set \mathbf{T}_c and PS set $\mathbf{P}_c \triangleq \bigcup_{d=1}^{N_T} \mathbf{P}_{c,d}$. Specifically, during the g -th slot with u -th user, the sweeping angle of the c -th RF chain is represented as $\bar{\psi}_{c,g,u} \in \mathbf{A}$. The angle set \mathbf{A} is defined as $\mathbf{A} = \left\{ \bar{\psi} \mid \bar{\psi} = -\frac{1}{2} + \frac{\bar{\varphi}}{N_S}, \bar{\varphi} = 0, 1, \dots, N_S - 1 \right\}$ with $N_S = GN_R$. The BS can subsequently sweep the signal from the sweeping angle.

We first optimize the TTD and PS to improve the sweeping performance for DFT-angle sequence. After the processing of PS set, TTD set, and CPP removal, the output signal with sweeping angle $\bar{\psi}_{c,g,u}$ is given by

$$r_{c,g,u}[i, \bar{\psi}_{c,g,u}] = \sum_{p=1}^P \sum_{d=1}^{N_T} \sum_{s=1}^{N_P} \alpha_{p,u}^g e^{-j2\pi f_c \left((a-1) \frac{\psi_{p,u}}{f_c} + t_{c,d}^g \right)} \times e^{j2\pi \kappa \left(i - \left(\frac{t_{c,d}^g}{T_s} + \ell_{p,u}^g + ((d-1)N_P + s - 1) \frac{\psi_{p,u}}{f_c T_s} - \frac{\nu_{p,u}}{f_c} \right) \right)^2} \times e^{j2\pi i \nu_{p,u} T_s} e^{j2\pi \Psi_{c,d,s}^g} + w_{c,g,u}[i], i = 0, \dots, M-1, \quad (27)$$

where $w_{c,g,u}[i] = \sum_{d=1}^{N_T} \sum_{s=1}^{N_P} \tilde{w}_{a,g,u}[i] * \bar{h}_{c,d,s}[i]$ and $\bar{h}_{c,d,s}[i] = \bar{h}_{c,d,s}[t] \Big|_{t=iT_s, \Psi_{c,d,s} = \Psi_{c,d,s}^g, t_{c,d} = t_{c,d}^g}$ with $a = (d-1)N_P + s$. The parameters $\Psi_{c,d,s}^g$ and $t_{c,d}^g$ respectively represent the values of $\Psi_{c,d,s}$ and the $t_{c,d}$ at the g -th slot. The de-chirp sequence is then derived by

$$\bar{r}_{c,g,u}[i, \bar{\psi}_{c,g,u}] = r_{c,g,u}[i, \bar{\psi}_{c,g,u}] \times e^{-j2\pi \kappa i^2} \approx \sum_{p=1}^P \sum_{d=1}^{N_T} \sum_{s=1}^{N_P} \alpha_{p,u}^g e^{j2\pi \kappa \left(\frac{t_{c,d}^g}{T_s} + \ell_{p,u}^g + ((d-1)N_P + s - 1) \frac{\psi_{p,u}}{f_c T_s} \right)^2} \times e^{j2\pi i \left(\nu_{p,u} T_s - 2\kappa \left(\frac{t_{c,d}^g}{T_s} + \ell_{p,u}^g + ((d-1)N_P + s - 1) \frac{\psi_{p,u}}{f_c T_s} \right) \right)} \times e^{-j2\pi \left(((d-1)N_P + s - 1) \psi_{p,u} + f_c t_{c,d}^g - \Psi_{c,d,s}^g \right)} + \bar{w}_{c,g,u}[i], \quad (28)$$

where $\bar{w}_{c,g,u}[i] = w_{c,g,u}[i] \times e^{-j2\pi \kappa i^2}$. The use of the approximation is based on the condition that $\kappa i \nu_{p,u} / f_c$ is typically negligible, $\forall i = 0, 1, \dots, M-1$. By N_A sweepings and using the DFT on $\bar{r}_{c,g,u}[i, \bar{\psi}_{c,g,u}]$ with time i , we can derive the DFT-angle sequence $R'_{c,g,u}[m, \bar{\psi}_{c,g,u}]$ as (29) at the top of the next page, where $R'_{c,g,u}[m, \bar{\psi}_{c,g,u}]$ is divided by M to normalize, $T_c = 1/f_c$, $m = -M/2, -M/2+1, \dots, M/2-1$ and $W_{c,g,u}[m]$ is the DFT of $\bar{w}_{c,g,u}[i]$ with time i .

2) *TDD-PS Net Design and Scattering Path Detection*: The BS determines the existence of a detection path by comparing the energy from the sweeping angle to a predefined threshold η . Without loss of generality, the angle of each scattering path is assumed to be unique for a specific user. As illustrated in , the BS can derive the detected angle set \mathbf{Q}_u if the the normalized peak $R'_{c,g,u}[m, \bar{\psi}_{c,g,u}]$ exceeds the threshold η as

$$\mathbf{Q}_u = \left\{ \bar{\psi}_{c,g,u} \mid \frac{\max(|R'_{c,g,u}[m, \bar{\psi}_{c,g,u}]|)}{\zeta_u[\bar{\psi}_{c,g,u}]} > \eta, \bar{\psi}_{c,g,u} \in \mathbf{A} \right\}, \quad (30)$$

where η is related to the probability of false alarm and miss rate [47]. $\zeta_u[\bar{\psi}_{c,g,u}]$ is the energy of received pilot expressed as

$$\zeta_u[\bar{\psi}_{c,g,u}] = \sum_{m=0}^{M-1} |R'_{c,g,u}[m, \bar{\psi}_{c,g,u}]|^2. \quad (31)$$

After G TDD slots, \mathbf{Q}_u can be obtained by sweeping all angles in the set \mathbf{A} . We denote P' as the number of elements in set \mathbf{Q}_u . Then, P' scattering paths can be detected after angle sweeping. However, the configuration of TTD and PS are still unknown for our receiving processing. Thus, We first analyze the configuration of TTD and PS such that the signal energy is maximized when the received signal comes from $\psi_{p,u} = -\bar{\psi}_{c,g,u}$. Specifically, from the p -th scattering path in (29), the value $\max(|R'_{c,g,u}[m, \bar{\psi}_{c,g,u}]|)$ can be maximized if TTD delay $t_{c,d}^g$ and PS phase shift $\Psi_{c,d,s}^g$ is given by

$$t_{c,d}^g = \tilde{t} + (d-1)N_P \bar{\psi}_{c,g,u} / f_c, \quad (32)$$

$$\Psi_{c,d,s}^g = (1-s) \left(1 + \frac{\kappa(M-1)}{T_s f_c} \right) \bar{\psi}_{c,g,u}, \quad (33)$$

where \tilde{t} is a constant to ensure $t_{c,d}$ is positive. From (29), there is a summation over the Dirichlet Sinc function about d and s in $R'_{c,g,u}[m, \bar{\psi}_{c,g,u}]$. Considering the power-focusing property of the Sinc function, a peak can be obtained only when the deviation between sweeping angle and real angle of scattering path angle is sufficiently small. Given detected angle $\bar{\psi}_{c,g,u} \in \mathbf{Q}_u$, the BS can derive the peak index by searching $|R[m, \bar{\psi}_{c,g,u}]|$ for $m = -M/2, -M/2-1, \dots, M/2-1$, i.e.,

$$m_{c,g,u}^{\nearrow} = \arg \max_{m=-M/2, -M/2+1, \dots, M/2-1} |R[m, \bar{\psi}_{c,g,u}]|, \bar{\psi}_{c,g,u} \in \mathbf{Q}_u \quad (34)$$

In order to enhance the performance of the estimation, we employ the Jocabsen estimator [48] to derive more refined

$$R'_{c,g,u}[m, \bar{\psi}_{c,g,u}] \approx \sum_{p=1}^P \sum_{d=1}^{N_T} \sum_{s=1}^{N_P} \alpha_{p,u}^g e^{-j2\pi(f_c t_{c,d}^g + (d-1)N_P \psi_{p,u}) \left(1 - \left((f_c t_{c,d}^g + (d-1)N_P \psi_{p,u}) \frac{1}{f_c T_s} + 2\ell_{p,u}^g\right) \frac{\kappa}{f_c T_s}\right)} \\ \times e^{j2\pi\kappa(\ell_{p,u}^g)^2} \frac{\sin\left(-\pi\left(m - M\nu_{p,u}T_s + 2M\kappa\left(\ell_{p,u}^g + (f_c t_{c,d}^g + (d-1)N_P \psi_{p,u}) \frac{1}{f_c T_s} + (s-1)\frac{\psi_{p,u}}{f_c T_s}\right)\right)\right)}{M \sin\left(-\frac{\pi}{M}\left(m - M\nu_{p,u}T_s + 2M\kappa\left(\ell_{p,u}^g + (f_c t_{c,d}^g + (d-1)N_P \psi_{p,u}) \frac{1}{f_c T_s} + (s-1)\frac{\psi_{p,u}}{f_c T_s}\right)\right)\right)} \\ \times e^{-j\pi\frac{M-1}{M}\left(m - M\nu_{p,u}T_s + 2M\kappa\left(\ell_{p,u}^g + (f_c t_{c,d}^g + (d-1)N_P \psi_{p,u}) \frac{1}{f_c T_s}\right)\right)} e^{-j2\pi\left(-\Psi_{c,d,s}^g + (s-1)\left(\psi_{p,u} + (M-1)\frac{\kappa\psi_{p,u}}{f_c T_s}\right)\right)} + W_{c,g,u}[m], \quad (29)$$

$$J(m_{c,g,u}^{\nearrow}, \bar{\psi}_{c,g,u}) = \Re \left\{ \frac{R_{c,g,u}[m_{c,g,u}^{\nearrow}, \bar{\psi}_{c,g,u} + \frac{1}{N_S}] - R_{c,g,u}[m_{c,g,u}^{\nearrow}, \bar{\psi}_{c,g,u} - \frac{1}{N_S}]}{2R_{c,g,u}[m_{c,g,u}^{\nearrow}, \bar{\psi}_{c,g,u}] - R_{c,g,u}[m_{c,g,u}^{\nearrow}, \bar{\psi}_{c,g,u} + \frac{1}{N_S}] - R_{c,g,u}[m_{c,g,u}^{\nearrow}, \bar{\psi}_{c,g,u} - \frac{1}{N_S}]} \right\} \frac{1}{N_S} - \bar{\psi}_{c,g,u}, \quad (35)$$

$$J'(m_{c,g,u}^{\nearrow}, \bar{\psi}_{c,g,u}) = m_{c,g,u}^{\nearrow} - \Re \left\{ \frac{R_{c,g,u}[m_{c,g,u}^{\nearrow} + 1, \bar{\psi}_{c,g,u}] - R_{c,g,u}[m_{c,g,u}^{\nearrow} - 1, \bar{\psi}_{c,g,u}]}{2R_{c,g,u}[m_{c,g,u}^{\nearrow}, \bar{\psi}_{c,g,u}] - R_{c,g,u}[m_{c,g,u}^{\nearrow} + 1, \bar{\psi}_{c,g,u}] - R_{c,g,u}[m_{c,g,u}^{\nearrow} - 1, \bar{\psi}_{c,g,u}]} \right\}, \quad (36)$$

$$R_{p',u}[m] \approx \sum_{d=1}^{N_T} \sum_{s=1}^{N_P} \alpha_{p',u}^g e^{-j2\pi((d-1)(\psi_{p',u} - \bar{\psi}_{c,g,u})N_P) \left(1 - \left((d-1)(\psi_{p',u} + \bar{\psi}_{c,g,u})N_P \frac{1}{f_c T_s} + 2\ell_{p',u}^g\right) \frac{\kappa}{f_c T_s}\right)} \\ \times e^{j2\pi\kappa(\ell_{p',u}^g)^2} \frac{\sin\left(-\pi\left(m - M\nu_{p',u}T_s + 2M\kappa\left(\ell_{p',u}^g + (d-1)(\psi_{p',u} + \bar{\psi}_{c,g,u})N_P \frac{1}{f_c T_s} + (s-1)\frac{\psi_{p',u}}{f_c T_s}\right)\right)\right)}{M \sin\left(-\frac{\pi}{M}\left(m - M\nu_{p',u}T_s + 2M\kappa\left(\ell_{p',u}^g + (d-1)(\psi_{p',u} + \bar{\psi}_{c,g,u})N_P \frac{1}{f_c T_s} + (s-1)\frac{\psi_{p',u}}{f_c T_s}\right)\right)\right)} \\ \times e^{-j\pi\frac{M-1}{M}\left(m - M\nu_{p',u}T_s + 2M\kappa\left(\ell_{p',u}^g + (d-1)(\psi_{p',u} + \bar{\psi}_{c,g,u})N_P \frac{1}{f_c T_s}\right)\right)} e^{-j2\pi(s-1)(\psi_{p',u} + \bar{\psi}_{c,g,u}) \left(1 + (M-1)\frac{\kappa\psi_{p',u}}{f_c T_s}\right)}, \quad (39)$$

angle and peak index as shown in (35) and (36), expressed at the top of this page. For the u -th user, we denote $\Phi_u = \{\hat{\psi}_{c,g,u} \mid \hat{\psi}_{c,g,u} = J(m_{c,g,u}^{\nearrow}, \bar{\psi}_{c,g,u}), \bar{\psi}_{c,g,u} \in \mathbf{Q}_u\}$ and $\mathbf{m}_u = \{\hat{m}_{c,g,u} \mid \hat{m}_{c,g,u} = J'(m_{c,g,u}^{\nearrow}, \bar{\psi}_{c,g,u}), \bar{\psi}_{c,g,u} \in \mathbf{Q}_u\}$ as angle set and peak index set, respectively. For the sake of illustration, we denote the actual scattering path angle closest to sweeping angle $-\bar{\psi}_{c,g,u}$ as $\psi_{p',u}$. Specifically, the sets Φ_u and \mathbf{m}_u^{\nearrow} can be respectively represented as

$$\Phi_u = \{\hat{\psi}_{1,u}, \hat{\psi}_{2,u}, \dots, \hat{\psi}_{P',u}\}, \quad (37)$$

$$\mathbf{m}_u^{\nearrow} = \{\hat{m}_{1,u}^{\nearrow}, \hat{m}_{2,u}^{\nearrow}, \dots, \hat{m}_{P',u}^{\nearrow}\}. \quad (38)$$

(37) and (38) can be summarized as following assumption:

Assumption 1: During the angle sweeping phase, the angle detected at the g -th slot with c -th RF chain, (i.e., $\bar{\psi}_{c,g,u} \in \mathbf{Q}_u$), is associated with the p' -th scattering path with angle $\psi_{p',u}$ for $p' = 1, 2, \dots, P'$.

3) *Analysis of Peak Index:* For ease of explanation, we use the p' -th path detected by the g -th TDD slot of the c -th RF chain as an example. By substituting (32) and (33) into (29), the noise-free sequence related to p' -th scattering path can be expressed as (39), at the top of this page, where the subscript c, g, u is omitted for simplification. Since the Dirichlet Sinc function $\text{sinc}(x)$ attaining its maximum value at $x = 0$, the relation between $\hat{m}_{p',u}^{\nearrow}$ and channel parameters can be expressed as

$$\hat{m}_{p',u}^{\nearrow} = -2\kappa M \left(\ell_{p',u}^g + \frac{(N_P - 1)\psi_{c,u}}{2f_c T_s} \right) + M\nu_{p',u}T_s \\ - (N_T - 1)(\bar{\psi}_{c,g,u} + \psi_{p',u})N_P \frac{\kappa M}{f_c T_s}, \quad (40)$$

where $\bar{\psi}_{c,g,u} \in \mathbf{Q}_u$. Equation (40) illustrates that the peak index $\hat{m}_{c,g}^{\nearrow}$ is determined by delay, Doppler and angle, which are unknown and desired parameters. Then, BS can derive the channel parameters using the peak index. We will introduce the details in Section III-C.

B. Beamforming Receiving for Down-chirp Pilot

In the beamforming receiving phase, the user transmits one single down-chirp pilot $\tilde{C}[i]$ at the $(G+1)$ -th slot. Let $\bar{\psi}_{c',G+1,u}$ denote the sweeping angle of the c' -th RF chain for down-chirp pilot, where $\cup_{c'=1}^{N_R} \bar{\psi}_{c',G+1,u} = -\Phi_u$. Then, the BS can receive down-chirp pilot from P scattering paths simultaneously. Similar to the analysis of up-chirp pilot, the TTD and PS can be optimized by following:

$$t_{c',d}^{G+1} = \tilde{t} + (d-1)N_P \bar{\psi}_{c',G+1,u} / f_c, \quad (41)$$

$$\Psi_{c',d,s}^{G+1} = (1-s) \left(1 - \frac{\kappa(M-1)}{T_s f_c} \right) \bar{\psi}_{c',G+1,u}. \quad (42)$$

The DFT-angle sequence for the down-chirp pilot can be expressed as (43), at the top of the next page, where $\ell_{p',u}^{G+1}$ is the delay for down chirp and can be expressed as

$$\ell_{p',u}^{G+1} = \ell_{p',u}^g - \frac{\nu_{p',u}}{f_c} (M + N_{CCP})(G - g + 1). \quad (44)$$

We omit the subscript $G+1$ of $\hat{R}_{c',u}$ for simplicity. For ease of exposition, we assume that the c' -th RF chain is align to the p' -th detected path for down-chirp case. The BS can derive the peak index of $\hat{R}_{c',u}[m, \bar{\psi}_{c',G+1,u}]$ as

$$m_{c',G+1,u}^{\nearrow} = \arg \max_{m=-M/2, -M/2+1, \dots, M/2-1} \left| \hat{R}_{c,u}[m, \bar{\psi}_{c',G+1,u}] \right|. \quad (45)$$

$$\begin{aligned}
\dot{R}_{c',u}[m, \bar{\psi}_{c',G+1,u}] &\approx \sum_{p'=1}^{P'} \sum_{d=1}^{N_T} \sum_{s=1}^{N_P} \alpha_{p',u}^{G+1} e^{-j2\pi((d-1)(\psi_{p',u} + \bar{\psi}_{c',G+1,u})N_P)} \left(1 + ((d-1)(\psi_{p',u} + \bar{\psi}_{c',G+1,u})N_P \frac{1}{f_c T_s} + 2\ell_{p',u}^{G+1}) \frac{\kappa}{f_c T_s}\right) \\
&\times e^{-j2\pi\kappa(\ell_{p',u}^{G+1})^2} e^{-j\pi \frac{M-1}{M} (m - M\nu_{p',u}T_s - 2M\kappa(\ell_{p',u}^{G+1} + (d-1)(\psi_{p',u} + \bar{\psi}_{c',G+1,u})N_P \frac{1}{f_c T_s}))} e^{-j2\pi(s-1)(\psi_{p',u} + \bar{\psi}_{c',G+1,u})} \left(1 - (M-1) \frac{\kappa\psi_{p',u}}{f_c T_s}\right) \\
&\times \frac{\sin\left(-\pi\left(m - M\nu_{p',u}T_s - 2M\kappa\left(\ell_{p',u}^{G+1} + (d-1)(\psi_{p',u} + \bar{\psi}_{c',G+1,u})N_P \frac{1}{f_c T_s} + (s-1)\frac{\psi_{p',u}}{f_c T_s}\right)\right)\right)}{M\sin\left(-\frac{\pi}{M}\left(m - M\nu_{p',u}T_s - 2M\kappa\left(\ell_{p',u}^{G+1} + (d-1)(\psi_{p',u} + \bar{\psi}_{c',G+1,u})N_P \frac{1}{f_c T_s} + (s-1)\frac{\psi_{p',u}}{f_c T_s}\right)\right)\right)} + W_{c',G+1,u}[m]. \quad (43)
\end{aligned}$$

Similar to (36) and (38), peak index set \mathbf{m}_u^{\searrow} is expressed as

$$\mathbf{m}_u^{\searrow} = \{\hat{m}_{1,u}^{\searrow}, \hat{m}_{2,u}^{\searrow}, \dots, \hat{m}_{P',u}^{\searrow}\}. \quad (46)$$

The relation between peak index $\hat{m}_{p',u}^{\searrow}$ and channel parameters can be expressed as

$$\hat{m}_{p',u}^{\searrow} = 2M\kappa\left(\ell_{p',u}^{G+1} + \frac{(N_P-1)\psi_{p',u}}{2f_c T_s}\right) + M\nu_{p',u}T_s, \quad (47)$$

where we assume $\bar{\psi}_{c',G+1,u} = -\hat{\psi}_{p',u} = -\psi_{p',u}$.

C. Channel Parameters Computation

By solving equations (26), (40), (44) and (47) under the premise of Assumption 1, Doppler and delay can be respectively derived by

$$\begin{aligned}
\hat{\nu}_{p',u} &= \left(\hat{m}_{p',u}^{\searrow} + \hat{m}_{p',u}^{\nearrow} + \frac{N_T-1}{f_c T_s}(\bar{\psi}_{c,g,u} + \hat{\psi}_{p',u})N_P M\kappa\right) \\
&\times \frac{1}{2MT_s - \frac{2\kappa M(M+N_{CCP})N_g}{f_c}}, \quad (48)
\end{aligned}$$

$$\begin{aligned}
\hat{\ell}_{p',u}^{G+1} &= -\frac{\hat{\psi}_{p',u}(N_P-1)}{2f_c T_s} - (N_T-1)(\bar{\psi}_{c,g,u} + \hat{\psi}_{p',u})\frac{N_P}{4f_c T_s} \\
&+ \frac{1}{4M\kappa}(\hat{m}_{p',u}^{\searrow} - \hat{m}_{p',u}^{\nearrow}) - \frac{(M+N_{CCP})N_g\hat{\nu}_{p',u}}{2f_c}, \quad (49)
\end{aligned}$$

where $N_g = (G-g+1)$ is the slot deviation. By substituting (47), (48), (49) into (43), we can derive the path gain as

$$\begin{aligned}
\hat{\alpha}_{p',u}^{G+1} &= \frac{\dot{R}_{c',u}[m_{c',G+1,u}^{\searrow}, \bar{\psi}_{c',G+1,u}]}{N_S} e^{j2\pi\kappa(\hat{\ell}_{p',u}^{G+1})^2} \\
&\times e^{j\pi \frac{M-1}{M} (m_{c',G+1,u}^{\searrow} - M\hat{\nu}_{p',u}T_s - 2M\kappa\hat{\ell}_{p',u}^{G+1})}, \quad (50)
\end{aligned}$$

where we assume $\bar{\psi}_{c',G+1,u} = -\psi_{p',u}$.

D. Complexity Analysis

1) *Algorithm Complexity*: For the processing of channel estimation, the computation be divided into analog part and digital part. The computational complexity of the analog part can be neglected, as it only involves the use of TTD and PS. The digital part consists of four parts, i.e., dechirp, DFT, path detection, peak searching and parameter computation. Dechirp is to multiply N samples with the local chirp sequence, with complexity expressed as $\mathcal{O}(M)$. The computation complexity of DFT can be expressed as $\mathcal{O}(M \log(M))$. Path detection determines whether the magnitude of N_A angle-domain samples exceeds a predefined threshold, which exhibits a complexity of $\mathcal{O}(N_A)$. The peak searching is to find the

maximum magnitude from M samples with the complexity expressed as $\mathcal{O}(M)$. The Jocabson estimator involves only simple addition and division operations, and its computational complexity is negligible. The channel parameters computation relies exclusively on elementary arithmetic, thereby rendering the computational complexity negligible. Thus, the overall complexity is dominated by $\mathcal{O}(N_A M \log(M) + N_A + 3M)$. In contrast, we list the complexities of the channel estimation algorithms in TABLE I based on grid searching [18] and sparse Bayesian learning (SBL) [49], where I represents the number of iterations.

TABLE I
COMPLEXITY OF DIFFERENT ALGORITHMS

Algorithm	Computation complexity
Grid searching-based [18]	$\mathcal{O}(N_A M \log N_A M + P N_A M + N_A M)$
SBL-based [49]	$\mathcal{O}(16I(MN_{RF})^2 M N_A)$
Proposed	$\mathcal{O}(N_A M \log(M) + N_A + 3M)$

2) *Pilot Cost*: Considering the pilot structure in Fig. 3, with respect to each user, BS is required to transmit $G+1$ chirp-based pilots, each with $M+N_{CCP}$ sampling points. Thus, the pilot costs can be expressed as $(G+1)(M+N_{CCP})$.

IV. PROPOSED DOWNLINK HYBRID PRECODING DESIGN

The doubly squint effect seriously destroys the sparsity of the DD-domain channel, which increases the complexity of the direct precoding in the DD domain. In this work, we consider a new hybrid precoding scheme using the channel parameters estimated in Section III. Equation (20) can be rewritten as (51), at the top of the next page. From (51), the effect of Doubly squint effect can be decomposed into phase shifts in DD domain and TF domain. Therefore, it is feasible to to compensate the phase shifts in DD and TF domains to realize precoding. Instead of direct precoding in the DD domain with convolution [50], we consider a hybrid precoding with digital part compensating the phase deviation in both DD domain and TF domain. To simplify notation, we denote $\{\hat{\tau}_{p',u}, \hat{\nu}_{p',u}, \hat{\psi}_{p',u}, \hat{\alpha}_{p',u}\}$ as the channel parameter used in our proposed hybrid precoding. The input-output relationship in (16) can be rewritten as

$$\begin{aligned}
y_u[k, \ell] &= \frac{1}{NM} h_{k,\ell}^{u,u} x_u[k, \ell] \\
&+ \frac{1}{NM} \sum_{k'=0}^{N-1} \sum_{\ell'=0}^{M-1} \sum_{u'=0, u' \neq u}^U h_{k,\ell}^{u,u'}[k', \ell'] x_{u'}[k', \ell'] \\
&+ \frac{1}{NM} \sum_{k'=0, k' \neq k}^{N-1} \sum_{\ell'=0, \ell' \neq \ell}^{M-1} h_{k,\ell}^{u,u}[k', \ell'] x_u[k', \ell'] + w_u[k, \ell], \quad (52)
\end{aligned}$$

$$\begin{aligned} \tilde{h}_{k,\ell}^{u,u'}[k',\ell'] &= \sum_{p=1}^P \sum_{c=1}^{N_R} \frac{\sqrt{\rho_c}}{NM} e^{j2\pi\nu_{p,u}\frac{\ell'}{M}} \sum_{n=0}^{N-1} \sum_{m=0}^{M-1} e^{j2\pi\left(\frac{n(k'-k)}{N} - \frac{m(\ell'-\ell)}{M}\right)} \alpha_{p,u} e^{-j2\pi\frac{m\ell_{p,u}}{M}} e^{j2\pi n\left(\frac{k_{p,u}}{N} + \frac{m}{\mu_{p,u}}\right)} \\ &\times \sum_{d=1}^{N_T} \sum_{s=1}^{N_P} e^{-j2\pi(((d-1)N_P+s-1)\psi_{p,u} + \ell_{c,d}f_c)\left(1 + \frac{m\Delta f}{f_c}\right)} e^{j2\pi\Psi_{c,d,s}} e^{j2\pi\nu_{p,u}\frac{\left(\ell_{c,d} + \ell_{p,u} + ((d-1)N_P+s-1)\frac{\psi_{p,u}}{f_c T_s}\right)T}{M}} \end{aligned} \quad (51)$$

$$\text{SINR}_{k,\ell} = \frac{\left|h_{k,\ell}^{u,u}[k,\ell]\right|^2}{\sum_{k'=0, k' \neq k}^{N-1} \sum_{\ell'=0, \ell' \neq \ell}^{M-1} \left|h_{k,\ell}^{u,u}[k',\ell']\right|^2 + \sum_{k'=0}^{N-1} \sum_{\ell'=0}^{M-1} \sum_{u' \neq u}^U \left|h_{k,\ell}^{u,u'}[k',\ell']\right|^2 + \sigma^2}, \quad (54)$$

where the first item corresponds to the desired signal, the second is inter-user interference the third refers to ISI, and the forth is AWGN in the DD domain with variance σ^2 . Therefore, the achievable rate per DD grid can be represented as

$$C_{k,\ell}^u = \log_2(1 + \text{SINR}_{k,\ell}), \quad (53)$$

where $\text{SINR}_{k,\ell}$ is the signal to interference plus noise ratio (SINR) of the DD grid $x_u[k,\ell]$, which can be represented as (54), at the top of this page. In order to maximize the achievable rate, we then optimize our proposed precoding method by maximizing the SINR in the following analysis.

From (20), the beam squint effect can be mitigate by configuring TTDs and PSs as

$$t_{c,d} = -\kappa N_P \hat{\psi}_{p',u}/f_c, \quad (55)$$

$$\Psi_{c,d,s} = (s-1)\hat{\psi}_{p',u}. \quad (56)$$

(55) and (56) illustrate that each RF chain is aligned to a specific angle [25]. This requirement is well-suited for the PDMA scheme [33], as it schedules user access based on the overlap of their scattering paths in the angle domain. By using the scheduling strategy of PDMA, the inter-user interference is negligible when the number of antenna is large enough. Thus, only the case of $u' = u$ is considered in (52).

In PDMA scheme, each RF chain can transmit signals to a unique scattering path with a specific user. We assume that the signal related to the p' -th path is precoded by the c' -th RF, where c' is mapping by $c' = \mathcal{M}(u, p')$. Considering that the DD-domain digital precoding $D_{c',u}[k',\ell']$ contains the mapping relationship between RF chain and scattering path, $D_{c',u}[k',\ell']$ can be simplified to

$$D_{c',u}[k',\ell'] = \begin{cases} 0, & c' \neq \mathcal{M}(u, p') \\ \bar{D}_{p',u}[k',\ell'], & c' = \mathcal{M}(u, p') \end{cases}, \quad (57)$$

where $\bar{D}_{p',u}[k',\ell']$ is used to compensate the phase deviation that related to k' and ℓ' . From (20) $\bar{D}_{p',u}[k',\ell']$ is given by

$$\bar{D}_{p',u}[k',\ell'] = e^{-j2\pi\hat{\nu}_{p',u}\frac{\ell'}{M}} \times \begin{cases} 1, & \ell' \in \mathcal{L}_{ICI}^{p',u} \\ e^{j2\pi\frac{k'}{N}}, & \ell' \in \mathcal{L}_{ISI}^{p',u} \end{cases}. \quad (58)$$

By using (58), $h_{k,\ell}^{u,u}[k',\ell']$ can be expressed as (59). Here, we define $\bar{\rho}_{p',u} = \rho_c$ to unify notation. Without loss of generality, we consider $e^{-j2\pi(s-1)\psi_{p',u}\left(\frac{m\Delta f - \nu_{p',u}}{f_c}\right)} \approx 1$ when N_T is large enough. Then, given $c' = \mathcal{M}(u, p')$, the remaining

phase shift associated with n and m can be compensated if TF precoding $B_{c'}[n, m]$ is given by

$$\begin{aligned} B_{c'}[n, m] &= \frac{\hat{\alpha}_{p',u}^*}{|\hat{\alpha}_{p',u}|} e^{-j2\pi\hat{\nu}_{p',u}\bar{\ell}_u T_s} e^{j2\pi\frac{m}{M}(\bar{\ell}_{p',u} + \bar{\ell}_u)} \\ &\times e^{-j2\pi n\left(\frac{k_{p',u}}{N} + \frac{m}{\mu_{p',u}}\right)}, \end{aligned} \quad (60)$$

where $\hat{k}_{p',u} = \hat{\nu}_{p',u}NT$, $\bar{\ell}_u$ is a constant and it is used to ensure that both index sets of ICI and ISI are suitable for all antennas. The index sets for ICI and ISI are formulated as (71) and (73), respectively. Here N_P and $\bar{\ell}_u$ are subject to the constraint as (72a) for all $1 \leq s \leq N_P$ and $\left|\frac{1}{\mu_{p',u}}\right| < \frac{\nu_{max}}{f_c}$.

Proof: Appendix B.

In order to derive the power factor $\sqrt{\rho_{c'}}$, we assume that the phase deviations introduced by different paths are compensated by the proposed hybrid precoding. Then, the power factor can be derived by maximum ratio combining (MRC). The optimal achievable rate per data symbol can be expressed as

$$C_{k,\ell}^u = \log_2 \left(1 + \frac{\left| \sum_{p'=1}^{P'} N_A \sqrt{\bar{\rho}_{p',u}} |\alpha_{p',u}| \right|^2}{\sigma^2} \right). \quad (61)$$

Let E_u denote total power of transmitted signal allocated to the u -th user. By using MRC, the optimal power factor $\sqrt{\rho_{c'}}$ can be derived as

$$\sqrt{\rho_{c'}} = \sqrt{\bar{\rho}_{p',u}} = \sqrt{\frac{E_u}{MN N_A}} \frac{|\hat{\alpha}_{p',u}|}{\sqrt{\sum_{p'=1}^P |\hat{\alpha}_{p',u}|^2}}. \quad (62)$$

V. SIMULATION RESULTS

In this section, the efficacy of the proposed method for channel estimation and hybrid precoding are evaluated. Unless otherwise stated, our main simulation parameters are given in TABLE II. The antenna spacing of BS is set to $\lambda_c/2$. The power of the multipath channel gain is normalized, i.e. $\sum_{p=1}^P |\bar{\alpha}_{p,u}|^2 = 1$. The signal-to-noise ratio (SNR) is expressed as $\text{SNR} = 10 \log(\sigma_y^2/\sigma_n^2)$, where σ_y^2 and σ_n^2 are the power of the received signal without noise and the power of AWGN, respectively. The performance metric of channel estimation is the normalized mean square error (NMSE) as

$$\text{NMSE}_{\mathbf{x}} = \mathbb{E} \left\{ \frac{\|\hat{\mathbf{x}} - \mathbf{x}\|^2}{\|\mathbf{x}\|^2} \right\}, \mathbf{x} = \boldsymbol{\alpha}_u, \boldsymbol{\tau}_u, \boldsymbol{\nu}_u, \quad (63)$$

$$h_{k,\ell}^{u,u}[k',\ell'] = \sum_{n=0}^{N-1} \sum_{m=0}^{M-1} \sum_{p'=1}^{P'} \sum_{s=1}^{N_P} e^{-j2\pi(s-1)\psi_{p',u}\left(\frac{m\Delta f - \nu_{p',u}}{f_c}\right)} \frac{N_T \sqrt{\rho_{p',u}}}{NM} \alpha_{p',u} e^{j2\pi\left(\frac{n(k'-k)}{N} - \frac{m(\ell'-\ell)}{M}\right)} \\ \times e^{j2\pi\nu_{p',u}\frac{\ell_{p',u}^T}{M}} \begin{cases} e^{-j2\pi\frac{m\ell_{p',u}}{M}} e^{j2\pi n\left(\frac{k_{p',u}}{N} + \frac{m}{\mu_{p',u}}\right)}, \ell' \in \mathcal{L}_{ICI}^{p',u} \\ e^{-j2\pi\frac{m\ell_{p',u}}{M}} e^{j2\pi(n-1)\left(\frac{k_{p',u}}{N} + \frac{m}{\mu_{p',u}}\right)}, \ell' \in \mathcal{L}_{ISI}^{p',u} \end{cases} \quad (59)$$

TABLE II
SIMULATION SETTINGS

Parameters	Value
Carrier frequency	30 GHz
Bandwidth	1 GHz
Number of subcarrier	2048
Subcarrier spacing	500 kHz
Number of path	4
propagation delay	[0, 10] Ts
UE speed	250 km/h
DoA of scattering path	[-90°, 90°]
Number of TTD line	8
Number of RF chain	4
SNR	15 dB
OTFS frame $M \times N$	2048 \times 128

where $\hat{\mathbf{x}}$ represents the estimation of \mathbf{x} , with its p -th item characterized by $\alpha_{p,u}$, $\tau_{p,u}$ and $\nu_{p,u}$. The achievable rate is the performance metric for the proposed hybrid precoding.

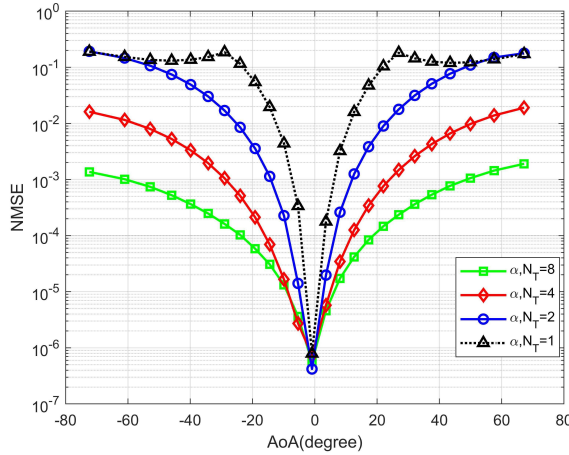


Fig. 5. The NMSE of α_u vs AoA at different numbers of TTD.

Fig. 5 illustrates the NMSE performance for path gain α_u at different TTD number, where the conditions with the TTD numbers N_T of 8, 4, 2 and 1 are considered. The number of scattering path is fixed as 1. As shown in Fig. 5, the NMSE decreases with the TTD number N_T increases. This is because the sum over Dirichlet Sinc function in (43) has deviation item $\frac{2M\kappa\psi_{p,u}}{f_c T_s}(s-1)$, for $s = 1, 2, \dots, N_P$. Considering $N_P = N_A/N_T$, the larger values of N_T lead to smaller values of N_P , which decrease the impact of the deviation item. In addition, the NMSE increases when the AoA deviates from 0°. This is because the deviation item $\frac{2M\kappa\psi_{p,u}}{f_c T_s}(s-1)$ is also a function of angle $\psi_{p,u}$, the larger $\psi_{p,u}$ leads to a higher deviation.

Fig. 6 shows the NMSE performance of τ_u , ν_u , α_u at different SNR. It compares two conditions: $N_T = 8$ and

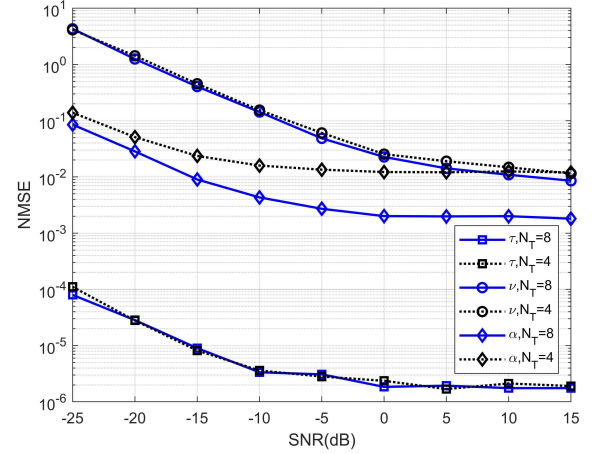


Fig. 6. The NMSE of τ_u , ν_u , α_u , vs SNR, slot deviation $N_g = 10$.

$N_T = 4$. The NMSE of τ_u , ν_u , α_u is observed to decrease with increasing SNR for both conditions. The increase of TTD number has a negligible effect on the NMSE for both τ_u and ν_u . However, the NMSE of α_u is notably lower when $N_T = 8$ compared to $N_T = 4$. This discrepancy arises because the estimation of τ_u and ν_u relies on the peak index of $R_{c,u}[m, \bar{\psi}_{c,g,u}]$ and $\hat{R}_{c',u}[m, \bar{\psi}_{c',G+1,u}]$, which is less sensitive to beam squint effect. The estimation of path gain α_u requires the maximum value of $\hat{R}_{c',u}[m, \bar{\psi}_{c',G+1,u}]$, which is more sensitive to beam squint effect.

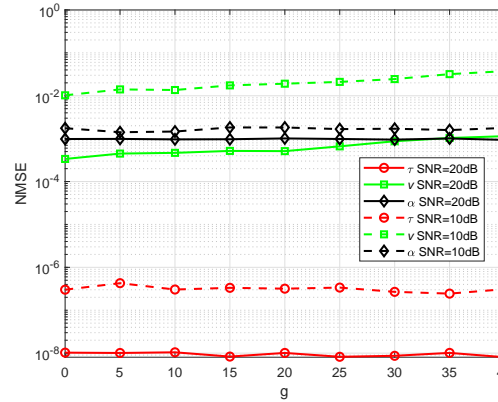


Fig. 7. The NMSE versus interval of reception g .

Fig. 7 illustrates the impact of the interval of reception g on the performance of NMSE. We consider that the beam squint effect are completely eliminated. From Fig. 7, the NMSE of Doppler estimation decreases as the interval between the up-chirp and down-chirp signals increases. This trend is attributed

to the fact that a larger interval leads to more significant variation in delay, thereby enhancing the ability to resolve delay variations, which resulting the Doppler shift. Meanwhile, the NMSE of delay estimation is not affected by the change of g . This is due to the high robustness of our super-resolution algorithm to small delay variations. Additionally, the NMSE of gain remains stable as g varies. This stability is because the path gain is more sensitive to delay variation rather than Doppler variation. When the accuracy of delay estimation is constant and the accuracy of Doppler estimation is slightly changed, the accuracy of path gain estimation remains almost constant.

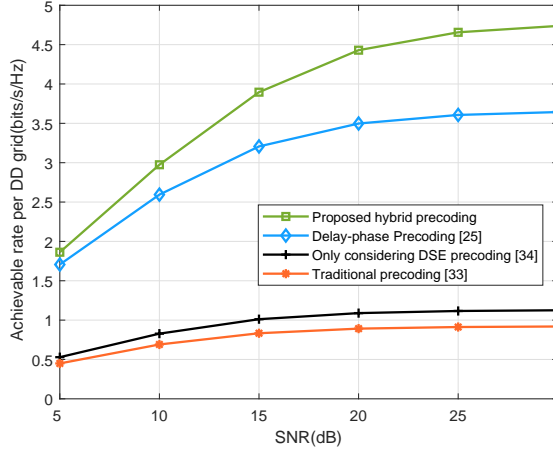


Fig. 8. Achievable rate per DD grid versus SNR.

The comparative analysis of the achievable rate per DD grid between the proposed hybrid precoding method and existing methods is depicted in Fig. 8. The alternative precoding schemes include only considering Doppler squint precoding [34], delay-phase precoding [25] and traditional precoding [33]. It is observed that the only considering Doppler squint precoding and traditional precoding exhibit lower achievable rates. This decline is primarily due to the beam squint effect, which significantly diminishes the array gain in wideband and large-scale antenna systems. Delay-phase precoding optimizes the array gain by compensating for the beam squint effect and has suboptimal performance. Our proposed precoding outperforms the others by effectively mitigating both the beam squint and Doppler squint effects, especially at high SNR conditions.

Fig. 9 presents a comparison of the average achievable rate per DD grid versus the bandwidth for different precoding schemes at a SNR of 20 dB. It is evident that the performance of only considering Doppler squint precoding and traditional precoding schemes exhibit a marked degradation at higher bandwidths. This is due to the fact that given a fixed subcarrier interval and symbol number N , an increase in bandwidth leads to an increase in the number of higher subcarriers. Thus resulting in a larger $M \times N$ causing a larger Doppler squint effect. In addition, the larger bandwidth leads to more severe beam squint effect. The enhancement of both Doppler squint effect and beam squint effect lead to a lower achievable rate as the

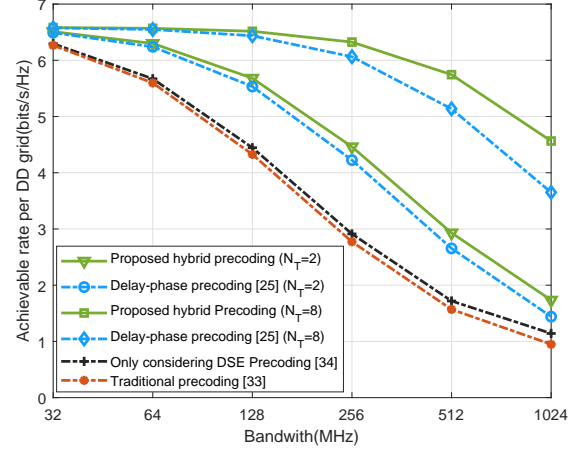


Fig. 9. Achievable rate per DD grid versus bandwidth.

bandwidth increases. Conversely, both delay-phase precoding and our proposed precoding demonstrate an enhancement in achievable rate performance with an increasing number of number of TTDs. Notably, the proposed precoding method demonstrates superior performance due to its consideration of both beam squint and Doppler squint effects. In addition, our analysis reveals that the proposed precoding scheme substantially enhances the achievable rate compared to delay-phase precoding, particularly when a large number of TDD elements are employed. However, this enhancement is less pronounced when the count of TDD elements is low.

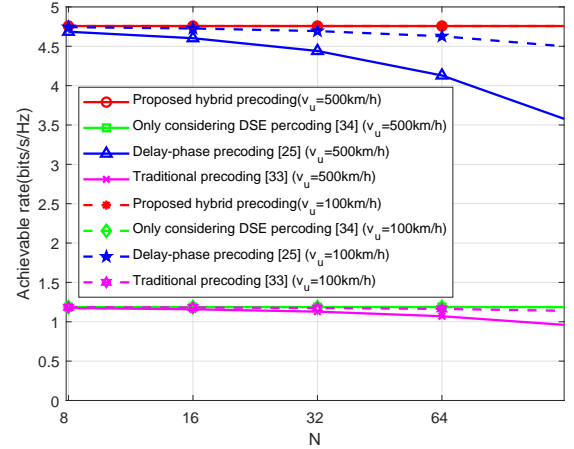


Fig. 10. Achievable rate per DD grid versus N .

Fig. 10 presents a comparison of the average achievable rates per DD grid for different precoding schemes and user velocities, where the SNR is 20 dB. The parameter N is associated with the duration of the OTFS frame. It is observed that precoding schemes that do not account for Doppler squint effect such as the Delay-phase precoding and traditional precoding, exhibit a decline in achievable rate as N increases, particularly at high velocities. This degradation is attributed to the Doppler squint effect, which is evident through the

factor $e^{\frac{j2\pi mn}{\mu_{p,u}}}$ in (20), leading to a phase deviation among different subcarriers and can be accumulated as N increases. In contrast, the performance of only considering Doppler squint precoding and the proposed precoding remains constant for all conditions. It illustrates that the effect of Doppler squint is eliminated. Moreover, as illustrated in Fig. 10, the beam squint effect tends to have a greater impact compared to the Doppler squint effect.

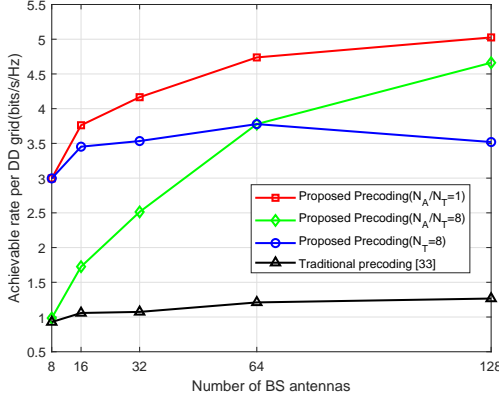


Fig. 11. Achievable rate per DD grid versus the number of BS antenna.

Fig. 11 illustrates the achievable rate per DD grid versus the number of BS antennas. When $N_A/N_T = 1$, the proposed precoding scheme can effectively eliminate both Doppler squint and beam squint, resulting in the maximum achievable rate. For the case where the number of TTD elements $N_T = 8$, the achievable rate initially increases with the number of antennas but eventually decreases as the number of antennas continues to grow. This is because when the number of antennas is small, the scattering paths cannot be distinguished in angle domain accurately, leading to significant inter-path interference. As the number of antennas increases, the resolution in the angle domain improves, thereby enhancing the achievable rate. However, when the number of antennas becomes excessively large, the beam squint effect becomes significant, resulting in a decrease in NMSE performance. As a result, as the number of antennas increases, the achievable rate progressively approaches the optimal value. Traditional precoding cannot eliminate the effect of beam squint, resulting in the achievable rate remains the lowest as the number of antennas increases.

Fig. 12 illustrates the achievable rate per DD grid versus the velocity of user, where the impact of bandwidth and subcarrier spacing on system performance are analyzed. From Fig. 12, when the bandwidth increases, the beam squint effect increases, which leads to the decrease of the achievable rate. On the other hand, when the bandwidth is fixed and the product $M \times N$ decreases, the achievable rate decreases. This is due to the fact that decreases in $M \times N$ leading to a reduction in symbol duration. This reduction in symbol duration mitigates the Doppler squint effect from the analysis in Section II.D. Furthermore, Fig. 12 shows that when $M \times N$ and velocity are constant, the impact of Doppler squint remains unchanged. This phenomenon validates our previous analysis.

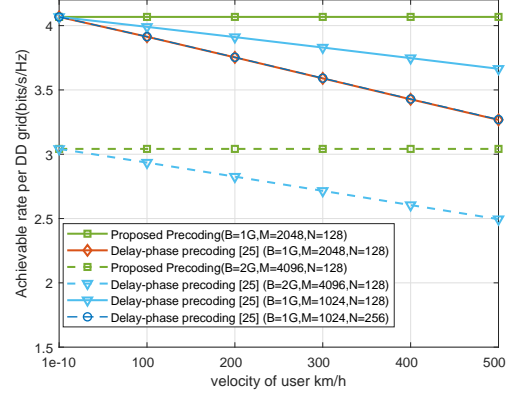


Fig. 12. Achievable rate per DD grid versus the velocity of user.

VI. CONCLUSION

This paper introduced a massive MIMO-OTFS system that accounts for the doubly squint effect, i.e., beam squint and Doppler squint effect. The input-output relationship was derived, which facilitated the analysis of doubly squint effect. Then, a channel estimation method with chirp pilot was proposed, where the parameters are determined by the peak index and peak value of DFT-angle sequences. For the receiving processing of the BS, a TTDs and PSs configuration was devised to mitigate the doubly squint effect. Additionally, a hybrid precoding scheme was introduced to compensate the phase shifts caused by doubly squint effect. Finally, simulation results substantiate the superiority and viability of the proposed methods.

It is worth noting that the channel model used in this work can still be regarded as a sparse model, where the number of scattering paths is finite and separable. However, the channel of practical scenarios may be non-sparse, leading to the spread of multipath components and the spread caused by doubly squint effect intertwined. Thus, the performance can be deteriorates severely in practical scenarios due to channel mismatch. Research on the doubly squint effect in non-sparse scenarios still requires further efforts to study.

APPENDIX A

PROOF OF DD-DOMAIN EQUIVALENT CHANNEL RESPONSE WITHOUT INVOLVING THE DIGITAL PRECODING

We first consider the case of ICI (i.e., $n' = n$). Given $B_c[n, m] = 1$ and $D_{c,u}[k, \ell] = 1, \forall c, u, m, n, k, \ell$, the DD-domain equivalent channel response can be represented as $\tilde{h}_{k,\ell}^{u,u'}[k', \ell']$, given by (64d). Here, (64b) is derived because the summation $\sum_{m'=0}^{M-1} e^{j2\pi \frac{m'(i-\ell')}{M}}$ is non-zero exclusively when $i - \ell' = 0$. From (64b), we can derive that $\tilde{h}_{k,\ell}^{u,u'}[k', \ell']$ is non-zero when τ is derived by

$$(1 + \mu_{p,u})\tau = \mu_{p,u} \left(\tau_{p,u} + t_{c,d} + (s-1) \frac{\psi_{p,u}}{f_c} \right) - n'T - \frac{i'T}{M}, \quad (65)$$

$$\tilde{h}_{k,\ell}^{u,u'}[k',\ell'] = \frac{\sqrt{\rho_c}}{MN} \sum_{n=0}^{N-1} \sum_{m=0}^{M-1} \sum_{d=1}^{N_T} \sum_{s=1}^{N_P} \sum_{p=1}^P \sum_{n'=0}^{N-1} \sum_{c=1}^{N_R} \int_{(n-n')T}^{(n-n'+1)T} \alpha_{p,u} |\mu_{p,u}| e^{-j2\pi\nu_{p,u}\mu_{p,u}(\tau-t_{c,d}-\tau_{p,u}-(a-1)\frac{\psi_{p,u}}{f_c})} e^{-j2\pi\tau m\Delta f} \\ \times e^{-j2\pi f_c(t_{c,d}+(a-1)\frac{\psi_{p,u}}{f_c})} \int e^{j2\pi\nu(\mu_{p,u}(\tau-t_{c,d}-\tau_{p,u}-(a-1)\frac{\psi_{p,u}}{f_c})+n'T+\tau+\frac{i'T}{M})} e^{j2\pi(\frac{n'k'}{N}-\frac{mi'}{M})} e^{-j2\pi\Psi_{c,d,s}} e^{j2\pi(-\frac{nk}{N}+\frac{m\ell}{M})} d\nu d\tau \quad (64a)$$

$$= \frac{\sqrt{\rho_c}}{MN} \sum_{n=0}^{N-1} \sum_{m=0}^{M-1} \sum_{d=1}^{N_T} \sum_{s=1}^{N_P} \sum_{p=1}^P \sum_{n'=0}^{N-1} \sum_{c=1}^{N_R} \int_{(n-n')T}^{(n-n'+1)T} \alpha_{p,u} |\mu_{p,u}| e^{-j2\pi\nu_{p,u}\mu_{p,u}(\tau-t_{c,d}-\tau_{p,u}-(a-1)\frac{\psi_{p,u}}{f_c})} e^{-j2\pi\tau m\Delta f} e^{j2\pi(-\frac{nk}{N}+\frac{m\ell}{M})} \\ \times e^{-j2\pi f_c(t_{c,d}+(a-1)\frac{\psi_{p,u}}{f_c})} \delta\left((1+\mu_{p,u})\tau - \left(\mu_{p,u}\left(t_{c,d}+\tau_{p,u}+(a-1)\frac{\psi_{p,u}}{f_c}\right) - n'T - \frac{i'T}{M}\right)\right) e^{j2\pi(\frac{n'k'}{N}-\frac{mi'}{M})} e^{-j2\pi\Psi_{a,b,c}} d\tau \quad (64b)$$

$$\stackrel{n'=n}{=} \sum_{n=0}^{N-1} \sum_{m=0}^{M-1} \sum_{d=1}^{N_T} \sum_{s=1}^{N_P} \sum_{p=1}^P \sum_{c=1}^{N_R} \frac{\sqrt{\rho_c}}{NM} \alpha_{p,u} \left| \frac{\mu_{p,u}}{\mu_{p,u}+1} \right| e^{-j2\pi m\Delta f(t_{c,d}+\tau_{p,u}+(a-1)\frac{\psi_{p,u}}{f_c})} e^{-j2\pi f_c(t_{c,d}+(a-1)\frac{\psi_{p,u}}{f_c})} \\ \times e^{j2\pi(\frac{\mu_{p,u}}{\mu_{p,u}+1}\nu_{p,u}+\frac{m\Delta f}{\mu_{p,u}+1})(t_{c,d}+\tau_{p,u}+(a-1)\frac{\psi_{p,u}}{f_c}+nT+\frac{i'T}{M})} e^{j2\pi(\frac{n'k'}{N}-\frac{mi'}{M})} e^{-j2\pi\Psi_{c,d,s}} e^{j2\pi(-\frac{nk}{N}+\frac{m\ell}{M})} \quad (64c)$$

$$\stackrel{i'=l'}{\approx} \sum_{n=0}^{N-1} \sum_{m=0}^{M-1} \sum_{p=1}^P \sum_{c=1}^{N_R} \sum_{d=1}^{N_T} \sum_{s=1}^{N_P} \frac{\sqrt{\rho_c}}{NM} \alpha_{p,u} e^{j2\pi(\frac{n(k'-k)}{N}-\frac{m(\ell'-\ell)}{M})} e^{-j2\pi(t_{c,d}f_c+((d-1)N_P+s-1)\psi_{p,u})(1+\frac{m\Delta f}{f_c})} \\ \times e^{j2\pi\Psi_{c,d,s}} e^{j2\pi\nu_{p,u}\frac{(\ell'+\ell_{p,u}+\bar{\ell}_{c,d}+((d-1)N_P+s-1)\frac{\psi_{p,u}}{f_cT_s})}{M}} e^{-j2\pi\frac{m\ell_{p,u}}{M}} e^{j2\pi n(\frac{k_{p,u}}{N}+\frac{m}{\mu_{p,u}})} \quad (64d)$$

$$h_{k,\ell}^{u',u'}[k',\ell'] = \frac{\hat{\alpha}_{p,u}^*}{|\hat{\alpha}_{p,u}|} \frac{N_T}{MN} \sum_{n=0}^{N-1} \sum_{m=0}^{M-1} \sum_{s=1}^{N_P} \sum_{p'=1}^{P'} \sum_{n'=0}^{N-1} \int_{(n-n')T}^{(n-n'+1)T} \alpha_{p',u'} |\mu_{p',u'}| e^{-j2\pi\mu_{p',u'}(\tau-\tau_{p',u'}-(s-1)\frac{\psi_{p',u'}}{f_c})} \nu_{p',u'} e^{-j2\pi\tau m\Delta f} \\ \times \int e^{j2\pi\nu(\mu_{p',u'}(\tau-\tau_{p',u'}-(s-1)\frac{\psi_{p',u'}}{f_c})+n'T+\tau+\frac{i'T}{M})} e^{j2\pi(\frac{n'k'}{N}-\frac{mi'}{M})} e^{-j2\pi n'\frac{\hat{k}_{p',u'}}{N}} e^{-j2\pi\hat{\nu}_{p',u'}\frac{(\ell'+\bar{\ell}_{u'})}{M}} e^{j2\pi(-\frac{nk}{N}+\frac{m\ell}{M})} d\nu d\tau \quad (67a)$$

$$\approx |\alpha_{p',u'}| \sum_{n=0}^{N-1} \sum_{m=0}^{M-1} \sum_{p'=1}^{P'} e^{-j2\pi\frac{m(\ell'-\ell-\bar{\ell}_{u'})}{M}} e^{j2\pi\frac{n(k'-k)}{N}} \quad (67b)$$

where $i' = \ell'$. Considering $(n-n')T < \tau < (n-n'+1)T$, equality (65) is valid only when we have

$$0 \leq \ell' < M - \left(\ell_{p',u'} + \ell_{c,d} + (a-1)\frac{\psi_{p',u'}M}{f_cT} \right) + \frac{M(n+1)}{\mu_{p',u'}}. \quad (66)$$

Then, the index set of ICI $\mathcal{L}_{ICI}^{p,u}$ can be derived by substituting $i' = \ell'$ into (66). The approximation in (64d) arises because $\mu_{p,u} \approx \mu_{p,u} + 1$.

The analysis of the ISI term is similar except for two differences. The first one is the integration range in equation (64b) extending from $(n-n'-1)T$ to $(n-n')T$. The second one is to employ $n' = [n-1]_N$ in equation (64c). With these considerations, we can derive the ISI index set for ℓ' as $\mathcal{L}_{ISI}^{p,u}$. Consequently, the DD-domain equivalent channel response without involving the digital precoding can be represented by equation (20).

APPENDIX B

PROOF OF PROPOSED HYBRID PRECODING METHOD

We first consider the case of ICI. By substituting (55), (56), (58) and (60) into (17), we can derive (67a), where, $i' = \ell' - \hat{\ell}_{p',u'} - \bar{\ell}_{u'} + \frac{Mn'}{\hat{\mu}_{p',u'}}$. Similar to the approach in Appendix A, the index set for i' is given by

$$0 \leq i' < M - \left(\ell_{p',u'} + (s-1)\frac{\psi_{p',u'}M}{f_cT} \right) + \frac{M(n+1)}{\mu_{p',u'}}. \quad (68)$$

Considering $i' = \ell' - \hat{\ell}_{p',u'} - \bar{\ell}_{u'} + \frac{Mn'}{\hat{\mu}_{p',u'}}$, the index set for l' can be represented as

$$\bar{\ell}_{u'} + \hat{\ell}_{p',u'} - \frac{Mn'}{\mu_{p',u'}} \leq \ell' < M - (s-1)\frac{\psi_{p',u'}}{f_cT_s} + \frac{M}{\mu_{p',u'}} + \bar{\ell}_{u'}. \quad (69)$$

Similarly, we can derive index set for ISI as

$$(s-1)\frac{\psi_{p',u'}}{f_cT_s} + \frac{M}{\mu_{p',u'}} + \bar{\ell}_{u'} \leq \ell' < \bar{\ell}_{u'} + \hat{\ell}_{p',u'} - \frac{Mn'}{\mu_{p',u'}}. \quad (70)$$

From (69) and (70), the index set for ICI and ISI is related to the PS index s . Since each RF chain connects N_P shifters, we expect the index set to be suitable for all phase shifters. With ℓ' being an integer in OTFS modulation, (69) can be simplified as

$$\mathcal{L}_{ICI}^{p',u'} = \left\{ \ell' \in \mathbb{N} : \hat{\ell}_{p',u'} + \bar{\ell}_{u'} - 1 \leq \ell' \leq M - 1 \right\}, \quad (71)$$

where we have

$$0 < -\frac{(s-1)\hat{\psi}_{p',u'}}{f_cT_s} + \frac{M}{\hat{\mu}_{p',u'}} + \bar{\ell}_{u'} < 1, \quad (72a)$$

$$0 < \bar{\ell}_{u'} - \frac{Mn'}{\hat{\mu}_{p',u'}} < 1, \quad (72b)$$

$\forall 1 \leq s \leq N_P, 0 \leq n' \leq N-1$ and $\left| \frac{1}{\hat{\mu}_{p',u'}} \right| < \frac{\nu_{max}}{f_c}$. Here, ν_{max} is the maximum Doppler shift. We omit the analysis of

ISI due to the space limitation. The index set for ISI can be expressed as

$$\mathcal{L}_{ISI}^{p',u'} = \left\{ \ell' \in \mathbb{N} : 1 \leq \ell' < \hat{\ell}_{p',u'} + \bar{\ell}_{u'} - 1 \right\}. \quad (73)$$

After that, we can get (67b), which does not contain path-related terms. That is, our precoding can compensate the phase deviation introduced by different paths. Considering $\bar{\ell}_{u'}$ is constant, the phase deviation introduced by $\bar{\ell}_{u'}$ can be easily compensated at receiver.

REFERENCES

- [1] Z. Pi and F. Khan, "An introduction to millimeter-wave mobile broadband systems," *IEEE Commun. Mag.*, vol. 49, no. 6, pp. 101–107, Jun. 2011.
- [2] F. Hasegawa, A. Taira, G. Noh, B. Hui, H. Nishimoto, A. Okazaki, A. Okamura, J. Lee, and I. Kim, "High-speed train communications standardization in 3GPP 5G NR," *IEEE Commun. Stand. Mag.*, vol. 2, no. 1, pp. 44–52, Mar. 2018.
- [3] W. Saad, M. Bennis, and M. Chen, "A vision of 6G wireless systems: Applications, trends, technologies, and open research problems," *IEEE Netw.*, vol. 34, no. 3, pp. 134–142, May/Jun 2020.
- [4] L. You, X. Gao, G. Y. Li, X.-G. Xia, and N. Ma, "BDMA for millimeter-wave/terahertz massive MIMO transmission with per-beam synchronization," *IEEE J. Sel. Area. Commun.*, vol. 35, no. 7, pp. 1550–1563, 2017.
- [5] X. Zhang, J. Tadrus, E. Everett, F. Xue, and A. Sabharwal, "Angle-of-arrival based beamforming for FDD massive MIMO," in *Proc. 49th Asilomar Conf. Signals, Sys. Compu.*, 2015, pp. 704–708.
- [6] M. Almoner, P. Mitran, and S. Boumaiza, "Investigation of the impact of zero-forcing precoding on the variation of massive MIMO transmitters' performance with channel conditions," *IEEE Microw. Wireless Compon. Lett.*, vol. 31, no. 6, pp. 802–804, Jun. 2021.
- [7] Y. Guo, R. Zhao, S. Lai, L. Fan, X. Lei, and G. K. Karagiannidis, "Distributed machine learning for multiuser mobile edge computing systems," *IEEE J. Sel. Top. in Signal Process.*, vol. 16, no. 3, pp. 460–473, Apr. 2022.
- [8] S. Zheng, C. Shen, and X. Chen, "Design and analysis of uplink and downlink communications for federated learning," *IEEE J. Sel. Area. Commun.*, vol. 39, no. 7, pp. 2150–2167, Jul. 2021.
- [9] D. Cai, P. Fan, Q. Zou, Y. Xu, Z. Ding, and Z. Liu, "Active device detection and performance analysis of massive non-orthogonal transmissions in cellular internet of things," *Sci. China Inf. Sci.*, vol. 65, no. 8, p. 182301, July 2022.
- [10] E. Torkildson, C. Sheldon, U. Madhow, and M. Rodwell, "Millimeter-wave spatial multiplexing in an indoor environment," in *Proc. IEEE Globecom Workshops*, 2009, pp. 1–6.
- [11] S. Ni, J. Zhao, H. H. Yang, and Y. Gong, "Enhancing downlink transmission in MIMO HetNet with wireless backhaul," *IEEE Trans. Veh. Technol.*, vol. 68, no. 7, pp. 6817–6832, Jul. 2019.
- [12] C. Xing, S. Ma, and Y.-C. Wu, "Robust joint design of linear relay precoder and destination equalizer for dual-hop amplify-and-forward MIMO relay systems," *IEEE Trans. Signal Process.*, vol. 58, no. 4, pp. 2273–2283, Apr. 2010.
- [13] X. Gao, L. Dai, and A. M. Sayeed, "Low RF-complexity technologies to enable millimeter-wave MIMO with large antenna array for 5G wireless communications," *IEEE Commun. Stand. Mag.*, vol. 56, no. 4, pp. 211–217, 2018.
- [14] Y. R. Ramadan and H. Minn, "Artificial noise aided hybrid precoding design for secure mmWave MISO systems with partial channel knowledge," *IEEE Signal Process. Lett.*, vol. 24, no. 11, pp. 1729–1733, Nov. 2017.
- [15] X. Gu, W. Zhang, and X. Bao, "Optimal design of subconnected hybrid structure for mmWave massive MIMO systems," in *Proc. IEEE 19th Int'l Conf. Commun. Technol. (ICCT)*, 2019, pp. 685–689.
- [16] B. Wang, F. Gao, S. Jin, H. Lin, G. Y. Li, S. Sun, and T. S. Rappaport, "Spatial-wideband effect in massive MIMO with application in mmWave systems," *IEEE Commun. Stand. Mag.*, vol. 56, no. 12, pp. 134–141, Aug. 2018.
- [17] B. Wang, F. Gao, G. Y. Li, S. Jin, and H. Lin, "Wideband channel estimation for mmWave massive MIMO systems with beam squint effect," in *Proc. IEEE Global Commun. Conf. (GLOBECOM)*, 2018, pp. 1–6.
- [18] B. Wang, F. Gao, S. Jin, H. Lin, and G. Y. Li, "Spatial- and frequency-wideband effects in millimeter-wave massive MIMO systems," *IEEE Trans. Signal Process.*, vol. 66, no. 13, pp. 3393–3406, Jul. 2018.
- [19] F. Gao, L. Xu, and S. Ma, "Integrated sensing and communications with joint beam-squint and beam-split for mmWave/THz massive MIMO," *IEEE Trans. Commun.*, vol. 71, no. 5, pp. 2963–2976, May 2023.
- [20] H. Yu, P. Guan, Y. Wang, and Y. Zhao, "Performance analysis and codebook design for mmWave beamforming system with beam squint," *IEEE Wireless Commun. Lett.*, vol. 10, no. 9, pp. 2013–2016, Sep. 2021.
- [21] P. Maity, S. Srivastava, S. Khatri, and A. K. Jagannatham, "Dictionary-learning (DL)-based sparse CSI estimation in multiuser terahertz (THz) hybrid MIMO systems under hardware impairments and beam-squint effect," *IEEE Access*, vol. 10, pp. 113 699–113 714, Oct. 2022.
- [22] Y. Shi, Y. Huang, X.-W. Tang, and Y. Xiao, "Channel estimation for wideband mmWave MIMO-OFDM system with beam squint effect," *IEEE Commun. Lett.*, vol. 28, no. 1, pp. 153–157, Jan. 2024.
- [23] M. Cai, K. Gao, D. Nie, B. Hochwald, J. N. Laneman, H. Huang, and K. Liu, "Effect of wideband beam squint on codebook design in phased-array wireless systems," in *Proc. IEEE Global Commun. Conf. (GLOBECOM)*, 2016, pp. 1–6.
- [24] R. Zhang, W. Hao, G. Sun, and S. Yang, "Hybrid precoding design for wideband THz massive MIMO-OFDM systems with beam squint," *IEEE Sys. J.*, vol. 15, no. 3, pp. 3925–3928, Jul. 2021.
- [25] L. Dai, J. Tan, Z. Chen, and H. V. Poor, "Delay-phase precoding for wideband THz massive MIMO," *IEEE Trans. Wireless Commun.*, vol. 21, no. 9, pp. 7271–7286, Mar. 2022.
- [26] Z. Huang, B. Zheng, and R. Zhang, "Transforming fading channel from fast to slow: Intelligent refracting surface aided high-mobility communication," *IEEE Trans. Wireless Commun.*, vol. 21, no. 7, pp. 4989–5003, Dec. 2022.
- [27] R. Hadani, S. Rakib, M. Tsatsanis, A. Monk, A. J. Goldsmith, A. F. Molisch, and R. Calderbank, "Orthogonal time frequency space modulation," in *Proc. IEEE Wireless Commun. Netw. Conf. (WCNC)*, 2017, pp. 1–6.
- [28] W. Shen, L. Dai, J. An, P. Fan, and R. W. Heath, "Channel estimation for orthogonal time frequency space (OTFS) massive MIMO," *IEEE Trans. Signal Process.*, vol. 67, no. 16, pp. 4204–4217, Aug. 2019.
- [29] T. Zemen, D. Lösch, M. Hofer, C. Pacher, and B. Rainer, "Orthogonally precoded massive MIMO for high mobility scenarios," *IEEE Access*, vol. 7, pp. 132 979–132 990, 2019.
- [30] B. C. Pandey, S. K. Mohammed, P. Raviteja, Y. Hong, and E. Viterbo, "Low complexity precoding and detection in multi-user massive MIMO OTFS downlink," *IEEE Trans. Veh. Technol.*, vol. 70, no. 5, pp. 4389–4405, May 2021.
- [31] W. Shao, S. Zhang, C. Zhong, X. Lei, and P. Fan, "Angle-delay-Doppler domain NOMA over massive MIMO-OTFS networks," in *Proc. IEEE/CIC Int. Conf. Commun. China, Chongqing, China*, 2020, pp. 74–79.
- [32] B. Shen, Y. Wu, J. An, C. Xing, L. Zhao, and W. Zhang, "Random access with massive MIMO-OTFS in LEO satellite communications," *IEEE J. Sel. Area. Commun.*, vol. 40, no. 10, pp. 2865–2881, Oct. 2022.
- [33] M. Li, S. Zhang, F. Gao, P. Fan, and O. A. Dobre, "A new path division multiple access for the massive MIMO-OTFS networks," *IEEE J. Sel. Area. Commun.*, vol. 39, no. 4, pp. 903–918, Apr. 2021.
- [34] X. Wang, X. Shi, J. Wang, and J. Song, "On the Doppler squint effect in OTFS systems over doubly-dispersive channels: Modeling and evaluation," *IEEE Trans. Wireless Commun.*, vol. 22, no. 12, pp. 8781–8796, Dec. 2023.
- [35] X. Wang, X. Shi, and J. Wang, "Sparse bayesian learning based off-grid estimation of OTFS channels with Doppler squint," *Tsinghua Sci. Technol.*, vol. 29, no. 6, pp. 1821–1828, Dec. 2024.
- [36] X. Wang, X. Shi, J. Wang, and J. Song, "Input-output relation and low-complexity receiver design for CP-OTFS systems with Doppler squint," in *2023 IEEE Globecom Workshops (GC Wkshps)*, 2023, pp. 539–544.
- [37] A. Liao, Z. Gao, D. Wang, H. Wang, H. Yin, D. W. K. Ng, and M.-S. Alouini, "Terahertz ultra-massive MIMO-based aeronautical communications in space-air-ground integrated networks," *IEEE J. Sel. Area. Commun.*, vol. 39, no. 6, pp. 1741–1767, Jun. 2021.
- [38] 3GPP, "Study on channel model for frequencies from 0.5 to 100 GHz," 3GPP, Technical Report 38.901, 2017. [Online]. Available: <https://www.3gpp.org/DynaReport/38901.htm>
- [39] Y. Ge, Q. Deng, P. C. Ching, and Z. Ding, "Receiver design for OTFS with a fractionally spaced sampling approach," *IEEE Trans. Wireless Commun.*, vol. 20, no. 7, pp. 4072–4086, Jul. 2021.
- [40] P. Raviteja, K. T. Phan, and Y. Hong, "Embedded pilot-aided channel estimation for OTFS in delay-Doppler channels," *IEEE Trans. Veh. Technol.*, vol. 68, no. 5, pp. 4906–4917, May 2019.

- [41] M. Nie, S. Li, D. Mishra, J. Yuan, and D. W. K. Ng, "Uplink multi-user OTFS: Transmitter design based on statistical channel information," *IEEE Trans. Commun.*, pp. 1–1, Dec. 2024 .
- [42] F. Liu, Y. Cui, C. Masouros, J. Xu, T. X. Han, Y. C. Eldar, and S. Buzzi, "Integrated sensing and communications: Toward dual-functional wireless networks for 6G and beyond," *IEEE J. Sel. Area. Commun.*, vol. 40, no. 6, pp. 1728–1767, Jun. 2022.
- [43] N. Petrov, "Range-Doppler circulating LFM for automotive MIMO radars," in *Proc. 20th Eur. Radar Conf. (EuRAD)*, 2023, pp. 169–172.
- [44] Y. Ye, J. Ma, S. Zhang, and O. A. Dobre, "Non-orthogonal downlink transmission for CSS-based LEO satellite iot," *IEEE Wireless Commun. Lett.*, pp. 1–1, Sep. 2024.
- [45] R. Zhang, J. Ma, S. Zhang, and O. A. Dobre, "Fractional chirp rate based CSS division multiple access over LEO satellite internet-of-things," *IEEE J. Sel.Top. in Signal Proces.*, pp. 1–15, Aug. 2024.
- [46] A. Bemani, N. Ksairi, and M. Kountouris, "AFDM: A full diversity next generation waveform for high mobility communications," in *Proc. IEEE Int. Conf. Commun. Workshops (ICC)*, 2021, pp. 1–6.
- [47] C.-L. Wang and H.-C. Wang, "On joint fine time adjustment and channel estimation for OFDM systems," *IEEE Trans. Wireless Commun.*, vol. 8, no. 10, pp. 4940–4944, Oct. 2009.
- [48] E. Jacobsen and P. Kootsookos, "Fast, accurate frequency estimators [DSP tips & tricks]," *IEEE Signal Process. Mag.*, vol. 24, no. 3, pp. 123–125, May 2007.
- [49] J. Fang, Y. Shen, H. Li, and P. Wang, "Pattern-coupled sparse Bayesian learning for recovery of block-sparse signals," *IEEE Trans. Signal Process.*, vol. 63, no. 2, pp. 360–372, Jan. 2015 .
- [50] S. Li, J. Yuan, P. Fitzpatrick, T. Sakurai, and G. Caire, "Delay-Doppler domain Tomlinson-Harashima precoding for OTFS-based downlink MU-MIMO transmissions: Linear complexity implementation and scaling law analysis," *IEEE Trans. Commun.*, vol. 71, no. 4, pp. 2153–2169, Apr. 2023 .